ACADEMIC PRESS

Available online at www.sciencedirect.com

SCIENCE DIRECT®

Journal of Computational Physics 185 (2003) 342–374

JOURNAL OF COMPUTATIONAL PHYSICS

www.elsevier.com/locate/jcp

Cures for the shock instability: Development of a shock-stable Roe scheme

Sung-soo Kim [a], Chongam Kim [a,b,*], Oh-Hyun Rho [a,b], Seung Kyu Hong [c]

[a] *Department of Aerospace Engineering, Seoul National University, Kwanka-Gu, Shilim-Dong, Seoul 151-742, Republic of Korea*
[b] *Institute of Advanced Aerospace Technology, Seoul National University, Republic of Korea*
[c] *Agency for Defense Development, Daejeon, Republic of Korea*

Received 17 October 2001; received in revised form 13 August 2002; accepted 16 October 2002

Abstract

This paper deals with the development of an improved Roe scheme that is free from the shock instability and still preserves the accuracy and efficiency of the original Roe's Flux Difference Splitting (FDS). Roe's FDS is known to possess good accuracy but to suffer from the shock instability, such as the carbuncle phenomenon. As the first step towards a shock-stable scheme, Roe's FDS is compared with the HLLE scheme to identify the source of the shock instability. Through a linear perturbation analysis on the odd–even decoupling problem, damping characteristic is examined and Mach number-based functions f and g are introduced to balance damping and feeding rates, which leads to a shock-stable Roe scheme. In order to satisfy the conservation of total enthalpy, which is crucial in predicting surface heat transfer rate in high-speed steady flows, an analysis of dissipation mechanism in the energy equation is carried out to find out the error source and to make the proposed scheme preserve total enthalpy. By modifying the maximum-minimum wave speed, the problem of expansion shock and numerical instability in the expansion region is also remedied without sacrificing the exact capturing of contact discontinuity. Various numerical tests concerned with the shock instability are performed to validate the robustness of the proposed scheme. Then, viscous flow test cases ranging from transonic to hypersonic regime are calculated to demonstrate the accuracy, robustness, and other essential features of the proposed scheme.

Keywords: Shock instability; Contact discontinuity; Expansion shock; Total enthalpy preservation; Roe's FDS; HLLE; RoeM scheme

1. Introduction

It is essential that a numerical representation of inviscid fluxes, namely a numerical flux function, should guarantee the high level of accuracy, efficiency, and robustness in computational fluid dynamics (CFD). In the last three decades, numerous numerical flux functions have been developed and much progress has been

* Corresponding author. Tel.: +82-2-880-1915; fax: +82-2-887-2662.
E-mail address: chongam@plaza.snu.ac.kr (C. Kim).

0021-9991/03/$ - see front matter
doi:10.1016/S0021-9991(02)00037-2

achieved. The Flux Difference Splitting (FDS) framework is one of the most successful groups among the various approaches to design numerical schemes and is widely used and studied. FDS schemes are generally based on the idea due to Godunov [1] and the Riemann problem is utilized locally. Godunov showed that after preparing piecewise constant initial data from cell-averaged flow values, numerical flux at a cell interface can be calculated through the exact solution of the Riemann problem. Although this strategy provides a way to obtain a good shock-capturing scheme, the Riemann problem is highly non-linear and has no closed form solution. In order to overcome this deficiency, many have tried to simplify the step of numerical flux calculation, which leads to the family of Godunov-type schemes or approximate Riemann solvers, such as Roe's FDS [2], HLLEM [3], Osher's FDS [4], and etc. These FDS schemes can capture contact discontinuity accurately and give good resolution for boundary layer in viscous flow calculation. Despite these advantages and the good shock-capturing property, some disastrous failings are also found in certain problems. This pathological behavior, usually represented as the 'carbuncle phenomenon', was first observed by Peery and Imlay [5] for blunt body computations with Roe's FDS. The carbuncle phenomenon refers to a protuberant shock profile obtained when a supersonic flow over a blunt body is calculated. Quirk [6] reported that approximate Riemann solvers generally suffer from such failings. After the carbuncle phenomenon was observed, many attempts were made to unveil the cause and to cure these failings. The attempts to cure the shock instability can be generally categorized into two groups. One is to use an alternative dissipative scheme in a hybrid manner and the other to employ an entropy fix.

Quirk [6] noticed that some schemes possessing the property of the good capturing of contact discontinuity show carbuncle phenomena while others free from carbuncle phenomena cannot capture contact discontinuity accurately. Thus, it is suggested that a dissipative scheme, such as HLLE, should be used in shock region while a less dissipative scheme, such as Roe's FDS, should be used elsewhere. In order to flag the cell interface where a dissipative scheme is needed, a pressure gradient sensor is used. Wada and Liou [7], by the same philosophy, suggest a similar flagging procedure but they use a sonic point. For a less dissipative scheme, AUSMDV is used and Hänel's FVS is used for a dissipative scheme. This cure turns out to be very efficient, as shown by the results reported in [6,7]. However, this approach always needs a proper counterpart that complements defects of the original flux function, and the selection of a proper numerical scheme itself is a critical problem. An inadequate counterpart may contaminate the accuracy of numerical solutions, especially in cases of high-speed flows.

An entropy fix to the linear wave field is a method to limit the minimum value of the wave speed, which is equivalent to the addition of extra numerical dissipation to damp out spurious oscillation. A fix on the linear wave field, however, is not a real entropy fix since only the non-linear waves should be fixed for the entropy condition to be satisfied. Peery and Imlay [5] propose an isotropic function for an entropy fix, and Lin [8] designs an anisotropic correction function using a pressure gradient sensor. Although this approach may successfully cure the carbuncle phenomenon, its performance always depends on the location and/or the amount of numerical dissipation added. Improper entropy fix may easily broaden shock wave profile and/or deteriorate boundary layer resolution. Thus, the development of a proper sensor that determines the location and the amount of numerical dissipation is crucial.

The two approaches to cure the shock instability problem, i.e., the use of dissipative numerical schemes and the employment of an entropy fix, are fundamentally the same in the sense that extra numerical dissipation is added to the original scheme in a way or another, and both need a detection procedure which usually involves a tuning coefficient.

So far, it is generally believed that a scheme that can capture contact discontinuity exactly, i.e., a scheme that has vanishing dissipation in stationary contact discontinuity, cannot avoid the shock instability, and the only way to prevent it is to add enough dissipation to damp out oscillation. However, Liou [9] observes that all the tested numerical functions that suffer from the shock instability have a term depending on pressure difference in the numerical mass flux while those free from the shock instability are independent of pressure difference in the numerical mass flux. Based on the numerical analysis and experiment, he suggests

the following conjecture: '*The condition* $D^{(P)} \neq 0, \forall M$, *in the mass flux is necessary for a scheme to develop, as t increases, the shock instability as manifested by the odd–even decoupling and carbuncle phenomena. On the other hand, the condition* $D^{(P)} = 0, \forall M$, *is sufficient for a scheme to prevent the shock instability from occurring*.' Here, $D^{(P)}$ stands for the dissipation term depending on pressure difference. This result indicates that it is possible to devise a FDS flux function free from the shock instability with vanishing dissipation in capturing stationary contact discontinuity. Xu [10] explains the shock instability using the Bernoulli equation and a convergent–divergent nozzle concept. According to his explanation, vanishing dissipation in the direction parallel to the shock and the contribution of pressure fluctuation to the numerical mass flux cause the shock instability. The analysis in [10] is in a qualitative agreement with Liou's conjecture in the sense that the pressure term in the numerical mass flux triggers the shock instability.

The present study aims at the design of a new Roe-based FDS flux function that is free from shock instability. Following Liou's conjecture and Xu's explanation, we focus on the pressure term in the numerical mass flux of Roe's FDS. In order to maintain the high level of robustness and accuracy, we impose that the newly developed flux function should satisfy the following criteria:

- The new flux function should be free from the shock instability without any tunable parameter.
- The new flux function should capture contact discontinuity exactly for the accurate resolution of boundary layer.
- Total enthalpy should be conserved for the accurate prediction of surface heat transfer rate in high-speed steady flows.
- Robustness in the expansion region should be substantially improved and entropy-violating expansion shock should be removed.

The present paper is organized as follows. After introduction, a list of the shock instability is briefly reviewed with some examples in Section 2. In Sections 3 and 4, we present the analysis procedure of Roe's flux function and propose Roe with Mach number-based function (RoeM) schemes. In Section 5, we present extensive numerical results and discuss properties of the schemes proposed in Section 4. In order to demonstrate various properties of the flux functions, we apply the proposed schemes to steady and unsteady problems. Finally, concluding remarks are given in Section 6.

2. Shock instability

In this section, we present the results of numerical experiments carried out using Roe's FDS on three examples. These tests, suggested by Quirk [6], include steady and unsteady cases and give some insight on the shock instability.

2.1. Quirk's test (odd–even decoupling)

Quirk [6] reports a tendency to occur odd–even decoupling along the planar shock that is aligned with the mesh in the middle of high-resolution simulation. In order to judge whether a scheme is shock-stable or not, he presents a simplified test case named 'odd–even decoupling,' a planar moving shock in a duct where a centerline grid is perturbed. It is considered that odd–even decoupling is connected with the carbuncle phenomenon, and any scheme that does not survive Quirk's test fails the blunt body problem. The computational mesh has a nominally uniform grid of 20×800 cells with unit spacing and the centerline of which is perturbed in the following manner:

$$Y_{i,j,\mathrm{mid}} = \begin{cases} Y_{j,\mathrm{mid}} + 10^{-4}, & \text{for } i \text{ even}, \\ Y_{j,\mathrm{mid}} - 10^{-4}, & \text{for } i \text{ odd}. \end{cases} \tag{1}$$

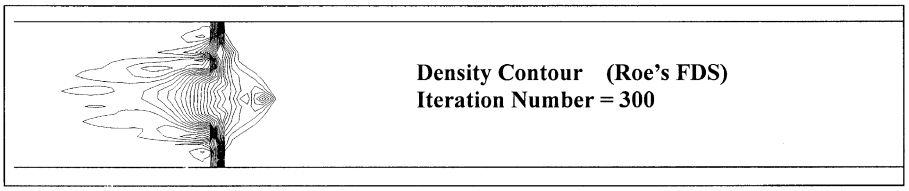

Fig. 1. Quirk's test: odd–even grid perturbation problem with a moving shock of $M_s = 6.0$.

This perturbation to the grid centerline promotes odd–even decoupling along the length of the shock. Compared to the perturbation used in [6] ($\Delta y = \pm 10^{-6}$), it is increased here to amplify odd–even decoupling phenomenon. The shock wave is traveling with a Mach number of $M_s = 6.0$. The computational result with Roe's FDS is presented in Fig. 1, which shows density contour after 300 iterations with CFL number 0.5. As the shock propagates downstream, perturbation grows from the center where the grid is perturbed, and eventually the planar shock breaks down.

2.2. The kinked Mach stem

Another kind of shock instability behavior is observed when a plane shock wave is reflected from a ramp to form a Double-Mach Reflection (DMR). The principal Mach stem is so severely kinked that an unphysical triple point appears. This pathological behavior, named 'the kinked Mach stem', is also unsteady phenomenon like 'odd–even decoupling' case. This test consists of a 30° ramp and a moving shock with $M_s = 5.5$. In Fig. 2(a), density contour with Roe's FDS on a 400×40 mesh is shown. The results are obtained with the first order spatial accuracy. First, the incident shock wave breaks down as in the case of 'odd–even decoupling', where the mesh is perfectly aligned with the shock wave. Also, the Mach stem protrudes like a beak at the wall, though the mesh is not aligned with the Mach stem. It is known that the shock instability is more likely to appear as the number of grid point increases. Figure 2(b) shows density contour on a 200×100 mesh. In this case, the incident shock wave does not show any shock instability behavior, while the Mach stem is still kinked.

2.3. The Carbuncle phenomenon (supersonic flow around a blunt body)

The carbuncle phenomenon was first reported by Peery and Imlay [5] for a flow around a blunt body. For steady state blunt body flow calculation, Godunov-type scheme admits a spurious solution in

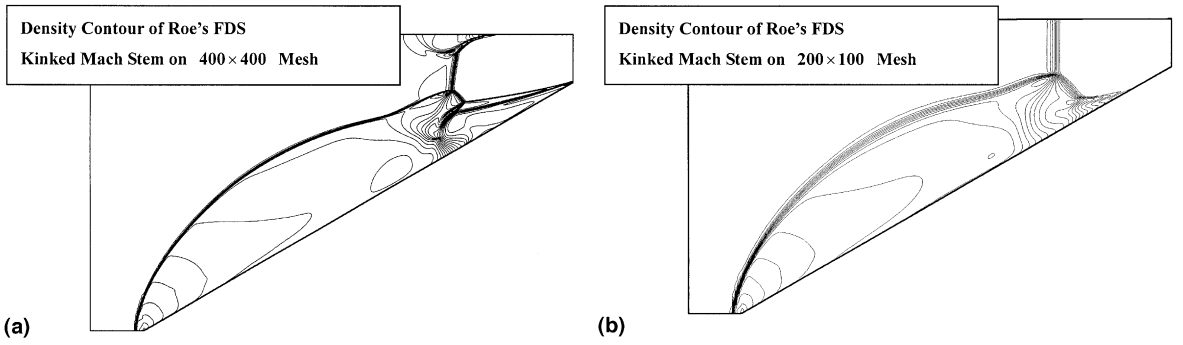

Fig. 2. Density contours of double Mach reflecting using Roe's FDS with first-order spatial accuracy.

which a protuberance grows ahead of the bow shock along the stagnation streamline. Figure 3 shows the pressure contour and the distribution of flow quantities along the stagnation line of a half-cylinder. Unsymmetrical flow behavior and the protuberance of the bow shock can be clearly seen. The free stream Mach number is 8.0, the mesh size is 65×113, and Roe's FDS is used with the first order accuracy.

2.4. Relation between the shock instability and pressure contribution

After the carbuncle phenomenon was first reported, many have found cases of the shock instability and have tried to save shock-capturing schemes from the disastrous phenomenon. As a result, some important characteristics were observed. First, it is noticed that the shock instability does not occur in one-dimensional calculation, i.e., shock instability is a multi-dimensional phenomenon. Also, it is found that dissipative schemes that cannot capture contact discontinuity, such as HLLE and van Leer's Flux Vector Splitting (FVS), are free from the shock instability. The instability is more likely to appear when the shock is aligned with the mesh. Roe's scheme or any other Godunov-type scheme that has the capability of capturing contact discontinuity exactly provides no dissipation in the direction parallel to the shock. On the other hand, schemes that cannot capture the contact discontinuity feed extra dissipation parallel to the shock and can avoid the disaster. Thus, many think that the addition of some dissipation may be the only recipe even if it has the potential to compromise the accuracy and/or the robustness of a solution. This idea is also supported by mathematical analysis. Through a linear analysis, Sanders et al. [11] argue that the shock instability is the result of inadequate crossflow dissipation provided by pure upwind schemes, and propose crossflow dissipation in order to eliminate the instability. Through a linear stability analysis, Gressier et al. [12,13] suggest that the exact capturing of contact discontinuity and strict stability cannot be simultaneously satisfied in any central scheme with matrix dissipation or any upwind scheme. And recently, through the odd–even decoupling analysis with manifold numerical schemes, Pandolfi and D'Ambrosio [14] maintain that the numerical schemes, which resolve contact discontinuity exactly, are not free from the shock instability.

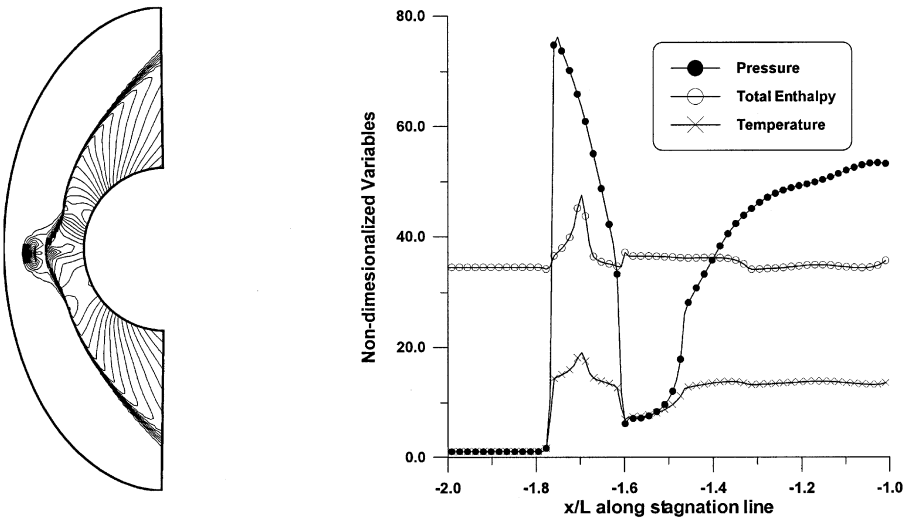

Fig. 3. Carbuncle phenomenon. Supersonic ($M_\infty = 8.0$) half-cylinder problem: pressure contour and shock profiles along the stagnation streamline.

However, some have paid attention to the role of the pressure term in the numerical mass flux in order to find the source of the shock instability. Comparing Roe's FDS with HLLE, Quirk [6] points out that if any scheme feeds the perturbation of pressure field to that of the density field, it will be afflicted by the shock instability. Recently, Liou [9] and Xu [10] presented qualitatively similar analyses. Their results agree with each other in the sense that the pressure term in the numerical mass flux plays a key role in invoking the shock instability. Xu explains that if pressure difference exists along the shock that is perfectly aligned with the mesh, the fluid will be pushed to the low-pressure region, where the flow velocity will be accelerated. This process makes the pressure in the low-pressure region even lower, as in the convergent nozzle. Since a Riemann-solver such as Roe's FDS add no dissipation to the contact discontinuity region and thus have no built-in mechanism to prevent this process, it will continue until the whole solution breaks down. Liou examines several numerical flux schemes and analyzes more rigorously the structure of numerical dissipation, finally reaching the conjecture that a non-zero pressure contribution in the numerical mass flux for all Mach numbers is a necessary condition for a scheme to develop the shock instability.

3. Cure for the shock instability

In this section, we present the cure for the shock instability of Roe's FDS with the damping and feeding rate control of density and pressure perturbation using the Mach number-based functions f and g.

3.1. Roe's flux function

The governing equations of inviscid flow in two-dimension are as follows:

$$\frac{\partial \mathbf{Q}}{\partial t}+\frac{\partial \mathbf{E}}{\partial x}+\frac{\partial \mathbf{G}}{\partial y}=0, \tag{2a}$$

where the state vector and flux vectors are

$$\mathbf{Q}=\begin{pmatrix}\rho\\ \rho u\\ \rho v\\ \rho e_t\end{pmatrix},\quad \mathbf{E}=\begin{pmatrix}\rho u\\ \rho u^2+p\\ \rho uv\\ \rho uH\end{pmatrix},\quad \mathbf{G}=\begin{pmatrix}\rho v\\ \rho uv\\ \rho v^2+p\\ \rho vH\end{pmatrix}. \tag{2b}$$

The equation of state has the form as follows:

$$p=(\gamma-1)\rho e=(\gamma-1)\rho\left(e_t-\frac{1}{2}(u^2+v^2)\right), \tag{3}$$

where the specific heat ratio γ is 1.4 for a perfect gas.

The numerical flux of Roe's FDS [2] at a cell interface is written as follows:

$$\mathbf{F}_{j+(1/2)}=\frac{1}{2}\left[\mathbf{F}_j+\mathbf{F}_{j+1}-|\hat{\mathbf{A}}|\Delta\mathbf{Q}\right], \tag{4a}$$

$$\mathbf{F}_j=\begin{pmatrix}\rho U\\ \rho uU+n_xp\\ \rho vU+n_yp\\ \rho UH\end{pmatrix}_j, \tag{4b}$$

$$|\hat{\mathbf{A}}|\Delta\mathbf{Q} = |\Delta\hat{\mathbf{F}}|_1 + |\Delta\hat{\mathbf{F}}|_2 + |\Delta\hat{\mathbf{F}}|_3 + |\Delta\hat{\mathbf{F}}|_4. \tag{4c}$$

U indicates contravariant velocity and n_x, n_y are unit normal vector components at the cell interface. $\hat{}$ means Roe-averaged value at the cell interface, which represents flow interaction between the j and the $j+1$ cell.

In Eq. (4a), the last term in the RHS is a matrix dissipation that characterizes Roe's FDS, which is represented as follows:

$$\begin{aligned}
|\Delta\hat{\mathbf{F}}|_1 &= |\hat{U}|\left(\Delta\rho - \frac{\Delta p}{\hat{c}^2}\right)\begin{pmatrix} 1 \\ \hat{u} \\ \hat{v} \\ \frac{\hat{u}^2+\hat{v}^2}{2} \end{pmatrix}, \quad |\Delta\hat{\mathbf{F}}|_2 = |\hat{U}|\hat{\rho}(n_y\Delta u - n_x\Delta v)\begin{pmatrix} 0 \\ n_y \\ -n_x \\ \hat{u}n_y - \hat{v}n_x \end{pmatrix}, \\
|\Delta\hat{\mathbf{F}}|_{3,4} &= |\hat{U} \pm \hat{c}|\left(\frac{\Delta p \pm \hat{\rho}\hat{c}\Delta U}{2\hat{c}^2}\right)\begin{pmatrix} 1 \\ \hat{u} \pm n_x\hat{c} \\ \hat{v} \pm n_y\hat{c} \\ \hat{H} \pm \hat{c}\hat{U} \end{pmatrix}.
\end{aligned} \tag{5}$$

$\hat{c}$ is the speed of sound based on Roe-averaged values, $|\Delta\hat{\mathbf{F}}|_1$ and $|\Delta\hat{\mathbf{F}}|_2$ are linear wave components that represent contact discontinuity, and $|\Delta\hat{\mathbf{F}}|_3$ and $|\Delta\hat{\mathbf{F}}|_4$ are non-linear wave components for shock waves or expansion waves. We will focus on the Δp in all linear and non-linear wave components, which is thought to be the source of the shock instability. In order to analyze the flux function readily, we rearrange it into another form.

In subsonic region,

$$\begin{aligned}
\mathbf{F}_{j+(1/2)} &= \frac{1}{2}\left[\mathbf{F}_j + \mathbf{F}_{j+1} - |\hat{\mathbf{A}}|\Delta\mathbf{Q}\right] = \frac{1}{2}\left[\mathbf{F}_j + \mathbf{F}_{j+1} - \hat{M}\hat{\mathbf{A}}\Delta\mathbf{Q} + \left(\hat{M}\hat{\mathbf{A}} - |\hat{\mathbf{A}}|\right)\Delta\mathbf{Q}\right] \\
&= \frac{1}{2}\left[\mathbf{F}_j + \mathbf{F}_{j+1} - \hat{M}(\mathbf{F}_{j+1} - \mathbf{F}_j) + (\hat{M}\hat{\mathbf{A}} - |\hat{\mathbf{A}}|)\Delta\mathbf{Q}\right].
\end{aligned} \tag{6a}$$

The eigenvalues of the matrix $\hat{M}\hat{\mathbf{A}} - |\hat{\mathbf{A}}|$ are

$$\lambda_{1,2} = \hat{c}(\hat{M}^2 - |\hat{M}|) = \hat{c}(\hat{M}^2 - 1) + \hat{c}(1 - |\hat{M}|) \text{ and } \lambda_{3,4} = \hat{c}(\hat{M}^2 - 1). \tag{6b}$$

In supersonic region,

$$\mathbf{F}_{j+(1/2)} = \mathbf{F}_j \text{ if } \hat{M} > 1 \text{ and } \mathbf{F}_{j+(1/2)} = \mathbf{F}_{j+1} \text{ if } \hat{M} < -1. \tag{6c}$$

Thus, Roe's FDS can be cast into the form as follows:

$$\mathbf{F}_{j+(1/2)} = \frac{1}{2}\left[\mathbf{F}_j + \mathbf{F}_{j+1} - \tilde{M}(\mathbf{F}_{j+1} - \mathbf{F}_j) + \hat{c}(\tilde{M}^2 - 1)\Delta\mathbf{Q} + \hat{c}(1 - |\tilde{M}|)\mathbf{B}\Delta\mathbf{Q}\right], \tag{7a}$$

where

$$\tilde{M} = \text{sign}(\hat{M}) \times \min(1., |\hat{M}|), \tag{7b}$$

$$\mathbf{B}\Delta\mathbf{Q} = \left(\Delta\rho - \frac{\Delta p}{\hat{c}^2}\right)\begin{pmatrix} 1 \\ \hat{u} \\ \hat{v} \\ \frac{\hat{u}^2+\hat{v}^2}{2} \end{pmatrix} + \hat{\rho}\begin{pmatrix} 0 \\ \Delta u - n_x\Delta U \\ \Delta v - n_y\Delta U \\ \hat{u}\Delta u + \hat{v}\Delta v - \hat{U}\Delta U \end{pmatrix}, \tag{7c}$$

and $\hat{M}$ is the normal Mach number computed with the contravariant velocity and $\hat{M} = \hat{U}/\hat{c}$.

In the above expression, it is noticed that Δp exists only in the last term $\mathbf{B}\Delta\mathbf{Q}$, which can be treated as a kind of anti-diffusion that enables Roe's FDS to capture contact discontinuity exactly but triggers the shock instability. This will be more obvious from the following comparison of Roe's FDS with HLLE scheme.

3.2. Cure for the shock instability

It is well known that HLLE scheme cannot capture contact discontinuity but is free from the shock instability. HLLE is also a Godunov-type solver but flow states separated by contact discontinuity are averaged in computing the numerical flux, which precludes the exact capturing of contact discontinuity. Except for the ignorance of contact discontinuity and the selection of wave speeds, however, there is no fundamental difference between HLLE and Roe's scheme. Thus, it will be beneficial to compare Roe's FDS with HLLE scheme. Similar to the form of Eq. (7a), the numerical flux of HLLE scheme can be rewritten as follows:

$$\mathbf{F}_{j+(1/2)} = \frac{1}{2}\left[\mathbf{F}_j + \mathbf{F}_{j+1} - \tilde{M}(\mathbf{F}_{j+1} - \mathbf{F}_j) + \hat{c}(\tilde{M}^2 - 1)\Delta\mathbf{Q}\right], \tag{8}$$

where Roe-averaged values are used for the non-linear wave speeds and $\tilde{M}$ is defined as Eq. (7b). Equation (8) is identical to Eq. (7a) except the last extra term $\mathbf{B}\Delta\mathbf{Q}$ in Eq. 7a, which enables Roe's FDS to capture contact discontinuity and triggers the shock instability.

In order to see the difference more concretely, we examine the structure of the numerical mass flux as follows:

$$\mathbf{F}^{(\rho)}_{j+(1/2)} = \frac{1}{2}\left[(\rho U)_{j+1} + (\rho U)_j\right] - \frac{1}{2}\left[D^{(\rho)}\Delta\rho + D^{(U)}\Delta U + \frac{D^{(p)}}{\hat{c}^2}\Delta p\right], \tag{9}$$

where dissipation term is expanded in terms of primitive variables. Then, dissipation coefficients $D^{(\rho)}$ and $D^{(p)}$ for Roe's FDS, HLLE, and Roe's FDS with an entropy fix to linear waves can be expressed as follows.

Roe's FDS:

$$D^{(\rho)}_{\text{Roe}} = \hat{c}|\hat{M}|, \quad D^{(p)}_{\text{Roe}} = \hat{c}(1 - |\hat{M}|). \tag{10a}$$

HLLE scheme with Roe-averaged wave speeds:

$$D^{(\rho)}_{\text{HLLE}} = \hat{c}, \quad D^{(p)}_{\text{HLLE}} = 0. \tag{10b}$$

Roe's FDS with an entropy fix to linear waves:

$$D^{(\rho)}_{\text{fix}} = \max(\hat{c}|\hat{M}|, \delta), \quad D^{(p)}_{\text{fix}} = \hat{c}(1 - |\hat{M}|), \tag{10c}$$

where the determination of δ depends on the method adopted.

From Eqs. (10a)–(10c) it can be seen that HLLE scheme has no pressure contribution to the numerical mass flux. This is in agreement with Liou's conjecture that the condition, $D^{(p)} = 0,$ for $\forall M$, is sufficient for a scheme to prevent the shock instability from occurring. It is noted that Roe's FDS with an entropy fix is also free from the shock instability but still has a pressure term in the numerical mass flux. Dissipation coefficients of Roe's FDS and Roe's FDS with an entropy fix, as functions of the Mach number, are shown in Fig. 4. It is noticed that as the Mach number goes to zero, the dissipation coefficient of density decreases to zero while the coefficient of pressure increases to unit. When an entropy fix is applied, the coefficient of density decreases as the Mach number goes to zero but remains at a finite value, which damps perturbation induced by pressure term.

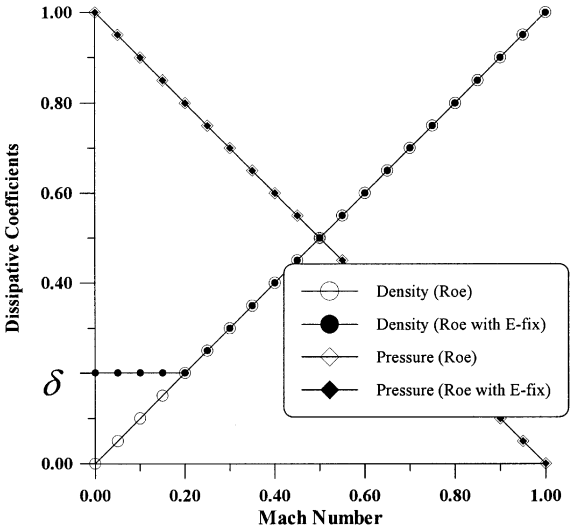

Fig. 4. Dissipation coefficients of density and pressure.

By solving the odd–even decoupling problem in [6], we can examine in detail how Roe's FDS, HLLE, and Roe's FDS with an entropy fix evolve sawtooth-type data and whether the perturbation grows or decays. We assume that the 2-D computational mesh is uniform and the discrete solution at time t^n is given by

$$\rho_j^n = \rho + \hat{\rho}^n, \quad p_j^n = p + \hat{p}^n, \quad u_j^n = u^0, \quad v_j^n = v^0, \tag{11a}$$

if j is even, and by

$$\rho_j^n = \rho - \hat{\rho}^n, \quad p_j^n = p - \hat{p}^n, \quad u_j^n = u^0, \quad v_j^n = v^0, \tag{11b}$$

if j is odd. Here, $\hat{\rho}^n$ and $\hat{p}^n$ are the amplitudes of sawtooth profiles for density and pressure fields, respectively. The amplitude at $n+1$ time level can be expressed as

$$\hat{\rho}^{n+1} = \left(1 - 2v_y \frac{D^{(\rho)}}{\hat{c}}\right)\hat{\rho}^n - \frac{2v_y}{\hat{c}^2}\frac{D^{(p)}}{\hat{c}}\hat{p}^n, \tag{12a}$$

$$\hat{p}^{n+1} = (1 - 2v_y)\hat{p}^n + 2v_y \frac{\gamma - 1}{\hat{c}^2}\left[\frac{\hat{u}^2 + \hat{v}^2}{2}\left(\frac{D^{(p)} + D^{(\rho)}}{\hat{c}} - 1\right) - \hat{v}^2\right]\hat{p}^n, \tag{12b}$$

where

$$v_y = \frac{c\Delta t}{\Delta y}.$$

When the velocity v^0 is equal to zero, i.e., the normal Mach number is zero, the amplitude at $n+1$ time level is expressed as follows:

For Roe's FDS:

$$\hat{\rho}^{n+1} = \hat{\rho}^n - \frac{2v_y}{\hat{c}^2}\hat{p}^n, \tag{13a}$$

$$\hat{p}^{n+1} = (1 - 2v_y)\hat{p}^n. \tag{13b}$$

For HLLE:

$$\hat{\rho}^{n+1} = (1 - 2v_y)\hat{\rho}^n, \tag{14a}$$

$$\hat{p}^{n+1} = (1 - 2v_y)\hat{p}^n. \tag{14b}$$

For Roe's FDS with entropy fix:

$$\hat{\rho}^{n+1} = \left(1 - 2v_y\frac{\delta}{\hat{c}}\right)\hat{\rho}^n - \frac{2v_y}{\hat{c}^2}\hat{p}^n, \tag{15a}$$

$$\hat{p}^{n+1} = \left(1 - 2v_y\right)\hat{p}^n + 2v_y\frac{\gamma - 1}{\hat{c}^2}\left[\frac{\hat{u}^2}{2}\left(\frac{\delta}{\hat{c}}\right)\right]\hat{p}^n. \tag{15b}$$

If there exists pressure perturbation, flow is driven by the pressure difference. In this process, pressure perturbation is damped, and mass is convected to the cell where pressure is low. As a result, pressure perturbation is turned into density perturbation. In the flow physics governed by the Euler equations, pressure difference has a role to drive flow but density and/or temperature difference is simply admitted as a solution because there is no physical diffusion mechanism.

Equations (13a) and (13b) show that Roe's FDS damps pressure perturbation but promotes density perturbation. Thus, if there exists a pressure perturbation source, then this will act as a density perturbation source after all. Xu [10] explains the relation between the shock instability and a pressure perturbation source as follows. If pressure difference exists along the shock that is perfectly aligned with the mesh, the fluid will be pushed to the low-pressure region, where the flow velocity will be accelerated. This process makes the pressure in the low-pressure region even lower, as in the convergent nozzle. After all, this will corrupt whole numerical solutions. Equations (14a) and (14b) show that HLLE scheme decouples the pressure field and density field. Pressure perturbation is damped but it does not affect the density field. And density perturbation is damped on its own mechanism. Equations (15a) and (15b), however, indicate that Roe's FDS with an entropy fix is in the intermediate state between Roe's FDS and HLLE scheme. Pressure perturbation convects the flow to the region where pressure is low, and this promotes density perturbation. But entropy fix has the role to damp density perturbation even when the normal Mach number is zero and to prevent this process from corrupting the whole numerical solution.

Thus, it may be interpreted that Liou's conjecture and entropy fix are all concerned about the balance of dissipations between pressure and density terms. The former requires $D^{(p)}$ to be zero, which results in the exclusion of pressure contribution to the numerical mass flux, while the latter restricts the minimum value of $D^{(\rho)}$ to counteract pressure contribution with the dissipation due to density difference, especially when the normal Mach number goes to zero.

It is known that the shock instability is more likely to appear when the shock is aligned with the mesh. If the shock is oblique, however, the shock instability is not to occur even though the shock is perfectly aligned with the mesh. When the velocity v^0 is not zero, i.e., the normal Mach number is not zero, the amplitude at $n + 1$ time level is expressed as follows:

For Roe's FDS:

$$\hat{\rho}^{n+1} = \left(1 - 2v_y|\hat{M}|\right)\hat{\rho}^n - \frac{2v_y}{\hat{c}^2}\left(1 - |\hat{M}|\right)\hat{p}^n, \tag{16a}$$

$$\hat{p}^{n+1} = (1 - 2v_y)\hat{p}^n - 2v_y(\gamma - 1)\hat{M}^2\hat{p}^n. \tag{16b}$$

In this case, pressure field still perturbs density field and a pressure perturbation source acts as a density perturbation source. But the transverse velocity acts as a numerical diffusion and damps the density perturbation. This diffusion mechanism results from the computational mesh with a finite size. After numerical flux is calculated and the fluid with a different density is convected, the fluid in the computational mesh is averaged, i.e., diffused to acquire mesh-averaged property. Thus, when the normal Mach number is not zero, density field has its own damping mechanism.

We calculate Quirk's test with a slightly different initial condition using Roe's FDS. Every condition is identical to Quirk's test in Section 2.1, but the transverse velocity component, i.e., the normal Mach number has the value of $\hat{M} \approx 0.15$ in terms of Roe-averaged value at the cell interface where the shock exists, and simple extrapolation is applied for boundary condition. Figure 5 shows density contour after 3400 iterations. It is observed that there is no symptom of the shock instability. When the transverse velocity exists, Eq. (16a) shows density field has its own damping mechanism. Thus, '$D^{(p)} = 0, \ \text{for} \ \forall M$' is considered too much severe as a restriction. Moreover, if $D^{(p)} = 0$ is always zero, the scheme that can capture contact discontinuity may have no mechanism to prevent pressure oscillation [15].

In order to balance the contribution of pressure to the numerical mass flux with density dissipation, $D^{(p)}$ is modified as follows:

$$D^{(p)}_{i,j+1/2} = \hat{c} f (1 - |\hat{M}|), \tag{17a}$$

$$f = \begin{cases} 1 & \hat{u}^2 + \hat{v}^2 = 0, \\ |\hat{M}|^h & \text{elsewhere}, \end{cases} \tag{17b}$$

$$h = 1 - \min\left(P_{i,j+(1/2)}, P_{i-(1/2),j}, P_{i+(1/2),j}, P_{i-(1/2),j+1}, P_{i+(1/2),j+1}\right), \tag{17c}$$

$$P_{i,j+(1/2)} = \min\left(\frac{p_{i,j}}{p_{i,j+1}}, \frac{p_{i,j+1}}{p_{i,j}}\right). \tag{17d}$$

Figure 6 shows the computational stencil for the function f. When we calculate the numerical flux at the $j + 1/2$ cell interface, the function h searches for the location where shock discontinuity exists. Since the shock instability is caused by the pressure perturbation parallel to the shock, the function h examines all the interfaces. Then the function f controls the pressure contribution according to the magnitude of the normal Mach number. Figure 7 shows the distribution of dissipative coefficients in the case where h has the value of 1. The function f and $D^{(p)}$ become zero when the normal Mach number is zero. It is noted that the dissipative coefficient of pressure is balanced with the dissipative coefficient of density. Since the control function f is dependent on the pressure ratio, the feeding rate may not be completely balanced with the damping rate all the time. We examine how Roe's FDS with the function f evolves sawtooth-type data.

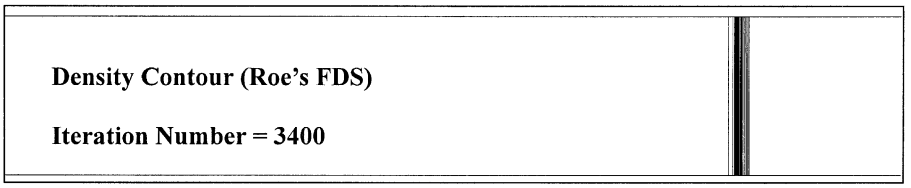

Fig. 5. Odd–even grid perturbation problem with a moving oblique shock of $M_s = 6.0$.

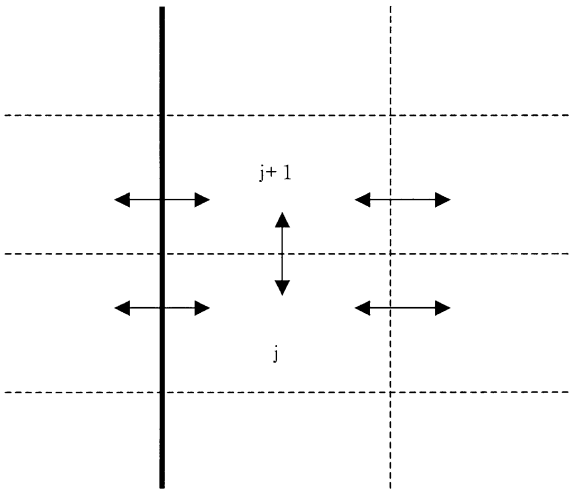

Fig. 6. A two-dimensional cell interface.

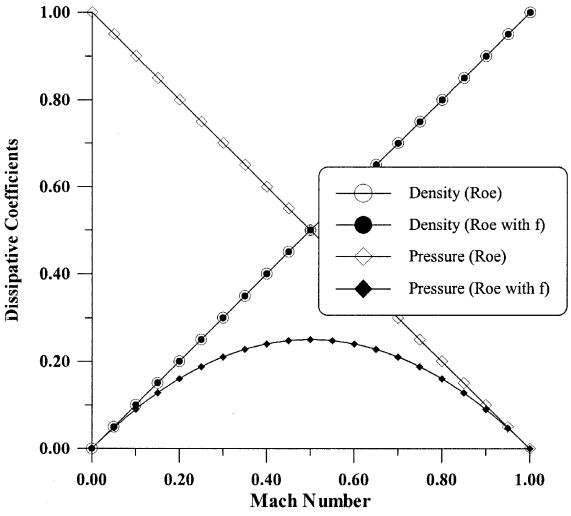

Fig. 7. Dissipation coefficients of pressure and density.

For Roe's FDS with the function f:

$$\hat{\rho}^{n+1} = \left(1 - 2v_y|\hat{M}|\right)\hat{\rho}^n - \frac{2v_y}{c^2}\left(1 - |\hat{M}|\right)f\hat{p}^n, \tag{18a}$$

$$\hat{p}^{n+1} = \left[1 - 2v_y f\{1 + (\gamma - 1)\hat{M}^2\}\right]\hat{p}^n. \tag{18b}$$

When the cell interface velocity is not zero, pressure and density are stable, i.e., density and pressure perturbation decay as time goes on. When the cell interface velocity is zero, pressure and density are neutrally stable, i.e., no growth and no decay. However, if pressure difference exists, Roe's FDS with the function f will generate

convective flow, and flow velocity across the cell interface will have the role to damp out perturbed property. From Eqs. (18a) and (18b), it can be observed that the rate at which density perturbation is damped out is equal to the dissipation coefficient of density, and the rate at which pressure field feeds density perturbation is proportional to the dissipation coefficient of pressure. Thus, the damping rate and the feeding rate can be controlled by the control of dissipation coefficients. Liou's conjecture and the above analysis show that the important is the balance between the damping rate and the feeding rate in density perturbation. The numerical flux of Roe's FDS with the function f defined in Eqs. (17a)–(17d) is given by

$$\mathbf{F}_{j+(1/2)} = \frac{b_1 \times \mathbf{F}_j - b_2 \times \mathbf{F}_{j+1}}{b_1 - b_2} + \frac{b_1 \times b_2}{b_1 - b_2}\Delta\mathbf{Q} - \frac{b_1 \times b_2}{b_1 - b_2} \times \frac{1}{1 + |\hat{M}|}\mathbf{B}\Delta\mathbf{Q}, \tag{19a}$$

$$\mathbf{B}\Delta\mathbf{Q} = \left(\Delta\rho - f\frac{\Delta p}{\hat{c}^2}\right)\begin{pmatrix} 1 \\ \hat{u} \\ \hat{v} \\ \frac{\hat{u}^2+\hat{v}^2}{2} \end{pmatrix} + \hat{\rho}\begin{pmatrix} 0 \\ \Delta u - n_x\Delta U \\ \Delta v - n_y\Delta U \\ \hat{u}\Delta u + \hat{v}\Delta v - \hat{U}\Delta U \end{pmatrix}, \tag{19b}$$

$$b_1 = \max(0, \hat{U} + \hat{c}), \qquad b_2 = \min(0, \hat{U} - \hat{c}). \tag{19c}$$

Equations (19a)–(19c) have the same form as HLLE scheme except for $\mathbf{B}\Delta\mathbf{Q}$ and the definitions of b_1 and b_2.

If pressure field is continuously and strongly perturbed, and the damping rate of density field in Eqs. (18a) and (18b) is not sufficient, such as in high-speed unsteady flow computations, it may not be effective with the function f only. However, in most numerical tests performed, the function f turns out to be sufficient to prevent the shock instability from occurring. And this confirms that shock instability has a strong dependence on the pressure contribution to the numerical mass flux. The case, which shows the role of the function f is not sufficient, is the double Mach reflection problem (see Section 5.2). It should be noted that AUSM+ scheme shows an unphysical triple point [13] even though it has the property of $D^{(p)} = 0$ for all Mach numbers. In this case, the damping rate in Eqs. (18a) and (18b) is small compared with the feeding rate of pressure perturbation generated from the computational mesh. This phenomenon is caused by flow unsteadiness. In order to cure this situation, a function g, which plays the role of increasing the damping rate of density field and controlling the perturbation in pressure field, is introduced as follows:

$$\mathbf{F}_{j+(1/2)} = \frac{b_1 \times \mathbf{F}_j - b_2 \times \mathbf{F}_{j+1}}{b_1 - b_2} + \frac{b_1 \times b_2}{b_1 - b_2}\Delta\mathbf{Q} - g\frac{b_1 \times b_2}{b_1 - b_2} \times \frac{1}{1 + |\hat{M}|}\mathbf{B}\Delta\mathbf{Q}, \tag{20a}$$

$$g = \begin{cases} |\hat{M}|^{1-\min\left(\frac{P_j}{P_{j+1}}, \frac{P_{j+1}}{P_j}\right)}, & \hat{M} \neq 0, \\ 1, & \hat{M} = 0. \end{cases} \tag{20b}$$

The function g checks whether the interface is contact discontinuity or not. When there is pressure gradient and there exists a transverse velocity, the function g increases the magnitude of the transverse velocity, i.e., damping rate. By solving the odd–even decoupling problem, we can examine the role of the function g.

For Roe's FDS with the function f and g:

$$\hat{\rho}^{n+1} = [1 - 2v_y(1 - g + g|\hat{M}|)]\hat{\rho}^n - \frac{2v_y}{c^2}(1 - |\hat{M}|)f\hat{p}^n, \tag{21a}$$

$$\hat{p}^{n+1} = (1 - 2v_y f)\rho^n + 2v_y(\gamma - 1)f\left[\frac{\hat{u}^2 + \hat{v}^2}{2\hat{c}^2}(1 - g)(1 - |\hat{M}|) - \hat{M}^2\right]p^n. \tag{21b}$$

Equations (21a) and (21b) show that the function g increases the transverse velocity according to the pressure difference, consequently increases the damping rate in density field as the pressure difference grows. As mentioned before, the function f has the role to control the feeding rate of pressure perturbation in the density field, especially when the normal Mach number is zero. In the case when pressure field is perturbed constantly and pressure difference grows in the calculation, the function g increases the damping rate and controls the growth of pressure perturbation simultaneously. Through this process, the damping rate is balanced with the feeding rate.

Recently, Pandolfi and D'Ambrosio [14] calculated supersonic blunt body flows and Quirk's problem using several upwind schemes in several grid systems, and observed some characteristics of the shock instability. Through these tests and odd–even decoupling analysis, it is shown that Roe's FDS and AUSM+ exhibit the shock instability but HLL does not, and maintained that those methods that explicitly deal with the contact surface display clear evidence of the carbuncle phenomenon and when such interaction is barely taken into account, or even totally ignored, no carbuncle instability occurs. It is clear that the shock instability has a close connection with the dissipation mechanism to capture contact discontinuity exactly. However, considering the fact that the carbuncle phenomenon is the case where small perturbations grow and destroy the shock profile, it is still unclear whether the results with AUSM+ in [14] really show the carbuncle phenomenon or they are just post-shock numerical oscillations which can usually seen in AUSM+ due to the location of sonic transition point with respect to the cell interface [16,17]. Also, the rationale for the categorization of light carbuncle prone schemes or carbuncle-free schemes suggests that the shock instability is indeed strongly dependent on the pressure term in the numerical mass flux, i.e., the feeding rate of pressure perturbations. In addition, the result due to Sanders et al. [11] shows that Roe's FDS with an entropy fix may still show the shock instability. It indicates that the shock instability is caused by the interaction between density field and pressure field.

4. Improved Roe scheme

Shock-stable Roe schemes with the Mach number-based functions (RoeM 1 and RoeM 2) that satisfy the requirements imposed in the Introduction are presented in this Section.

4.1. Total enthalpy conservation

It is known that Roe's FDS does not preserve total enthalpy in inviscid steady flow. Jameson [18] shows that the error source of total enthalpy is the discrepancy between the convective terms in the flux vector that contains ρH and the state vector that includes ρe_t in the energy equation. It is also suggested this defect can be remedied by introducing a modified state vector that contains ρH.

Some modification is needed in order for the modified Roe scheme in Section 3 to preserve total enthalpy. The dissipation of the continuity equation and energy equation in subsonic region is given by

$$\begin{bmatrix} D_{\text{continuity}} \\ D_{\text{energy}} \end{bmatrix} = \Delta\rho|\hat{M}| \begin{bmatrix} \hat{c} \\ \frac{\hat{c}}{2}\hat{q}^2 \end{bmatrix} + f\Delta\rho \begin{bmatrix} \frac{1}{\hat{c}} - \frac{|\hat{M}|}{\hat{c}} \\ \frac{1}{\hat{c}}\hat{U}^2 + \frac{\hat{H}}{\hat{c}} - \frac{1}{2\hat{c}}\hat{q}^2 - \frac{1}{2\hat{c}}\hat{q}^2(|\hat{M}| - 1) \end{bmatrix} + \Delta u|\hat{M}| \begin{bmatrix} 0 \\ \hat{\rho}\hat{c}\hat{u} \end{bmatrix} + \Delta v|\hat{M}| \begin{bmatrix} 0 \\ \hat{\rho}\hat{c}\hat{v} \end{bmatrix} + \Delta U \begin{bmatrix} \hat{\rho}\hat{M} \\ \hat{\rho}\hat{H}\hat{M} - \hat{\rho}\hat{c}^2\hat{M}(|\hat{M}| - 1) \end{bmatrix}. \tag{22}$$

In order for numerical flux to preserve total enthalpy, the following condition, which was introduced by Hänel [19], should be satisfied:

$$D_{\text{energy}} = D_{\text{continuity}} \times H. \tag{23}$$

Equation (22) can be rearranged for total enthalpy to appear explicitly as follows:

$$\begin{bmatrix} D_{\text{continuity}} \\ D_{\text{energy}} \end{bmatrix} = \hat{c}\Delta\rho|\hat{M}|\begin{bmatrix} 1 \\ \hat{H} \end{bmatrix} + f\left(\frac{1}{\hat{c}} - \frac{|\hat{M}|}{\hat{c}}\right)\Delta p\begin{bmatrix} 1 \\ \hat{H} \end{bmatrix} + \hat{\rho}\hat{M}\Delta U\begin{bmatrix} 1 \\ \hat{H} \end{bmatrix} + \hat{\rho}\hat{c}|\hat{M}|\begin{bmatrix} 0 \\ \Delta H \end{bmatrix}$$
$$+ f\Delta p\begin{bmatrix} 0 \\ \frac{\hat{U}^2}{\hat{c}} - \hat{c}|\hat{M}| \end{bmatrix} - \Delta U\begin{bmatrix} 0 \\ \hat{c}^2\hat{\rho}(|\hat{M}| - 1)\hat{M} \end{bmatrix}. \tag{24}$$

Equation (24) shows that the last two terms are the error sources. Although the fourth term on the right-hand side in Eq. (24) does not satisfy the condition of Eq. (23), ΔH becomes zero when the total enthalpy is conserved. Thus, total enthalpy conservation is satisfied by the elimination of the last two terms. Then, the modified Roe scheme preserving total enthalpy can be expressed as

$$\mathbf{F}_{j+(1/2)} = \frac{b_1 \times \mathbf{F}_j - b_2 \times \mathbf{F}_{j+1}}{b_1 - b_2} + \frac{b_1 \times b_2}{b_1 - b_2}\Delta\mathbf{Q}^* - \frac{b_1 \times b_2}{b_1 - b_2} \times \frac{1}{1 + |\hat{M}|}\mathbf{B}\Delta\mathbf{Q}, \tag{25a}$$

$$\Delta\mathbf{Q}^* = \Delta\begin{pmatrix} \rho \\ \rho u \\ \rho v \\ \rho H \end{pmatrix}, \quad \mathbf{B}\Delta\mathbf{Q} = \left(\Delta\rho - f\frac{\Delta p}{\hat{c}^2}\right)\begin{pmatrix} 1 \\ \hat{u} \\ \hat{v} \\ \hat{H} \end{pmatrix} + \hat{\rho}\begin{pmatrix} 0 \\ \Delta u - n_x\Delta U \\ \Delta v - n_y\Delta U \\ \Delta H \end{pmatrix}, \tag{25b}$$

$$b_1 = \max(0, \hat{U} + \hat{c}), \quad b_2 = \min(0, \hat{U} - \hat{c}). \tag{25c}$$

4.2. Expansion shock, instability in the expansion region

Another defect of Roe's FDS is the appearance of expansion shock. Roe's FDS does not have a built-in mechanism to distinguish expansion shock from compression shock. Thus, it admits expansion shock as a solution that violates the entropy condition. Also, in a highly energetic flow, Roe's FDS often yields physically unacceptable values, such as negative density and/or negative temperature. This robustness issue concerns the positivity condition. In order to overcome this drawback, an entropy fix is widely used. The entropy fix generally enables Roe's scheme to resolve expansion fan and helps to improve the robustness. Einfeldt et al. [3] show that no Godunov-type scheme based on a linearized Riemann solution is positively conservative, and explain that the reason for the failure of Roe's FDS is that the numerical signal velocities of Roe's Riemann solver underestimate the physical signal velocities. As a remedy, the numerical signal velocity at a cell interface is computed by incorporating the values at neighboring cells and eigenvalues of the dissipation matrix are re-defined, which leads to the design of HLLEM scheme. HLLEM does not require an entropy fix to detect expansion shock and does not suffer from the instability occurred in a highly energetic flow. The numerical flux of HLLEM can be cast in the following form:

$$\mathbf{F}_{j+(1/2)} = \frac{b_1 \times \mathbf{F}_j - b_2 \times \mathbf{F}_{j+1}}{b_1 - b_2} + \frac{b_1 \times b_2}{b_1 - b_2}\Delta\mathbf{Q} - \frac{b_1 \times b_2}{b_1 - b_2} \times \delta\left[\left(\Delta\rho - \frac{\Delta p}{\hat{c}^2}\right)\begin{pmatrix} 1 \\ \hat{u} \\ \hat{v} \\ \frac{\hat{u}^2 + \hat{v}^2}{2} \end{pmatrix}\right.$$
$$\left. + \hat{\rho}\begin{pmatrix} 0 \\ \Delta u - n_x\Delta U \\ \Delta v - n_y\Delta U \\ \hat{u}\Delta u + \hat{v}\Delta v - \hat{U}\Delta U \end{pmatrix}\right], \tag{26a}$$

$$\delta = \frac{\hat{c}}{|\bar{U}| + \hat{c}}, \qquad |\bar{U}| = \left| \frac{b_r + b_l}{2} \right|, \tag{26b}$$

$$b_r = \max(\hat{U} + \hat{c}, U_{j+1} + c_{j+1}), \quad b_l = \min(\hat{U} - \hat{c}, U_j - c_j), \tag{26c}$$

$$b_1 = \max(0, \hat{U} + \hat{c}, U_{j+1} + c_{j+1}), \quad b_2 = \min(0, \hat{U} - \hat{c}, U_j - c_j). \tag{26d}$$

In the above expression, δ is a positive parameter that controls the amount of anti-diffusion in the linear field, which corresponds to $1/(1 + |\hat{M}|)$ in Eqs. (25a)–(25c). Simply employing the definitions of b_1 and b_2 in Eqs. (26a)–(26d) the modified Roe's FDS of Eqs. (25a)–(25c) can be re-formulated as follows:

$$\mathbf{F}_{j+(1/2)} = \frac{b_1 \times \mathbf{F}_j - b_2 \times \mathbf{F}_{j+1}}{b_1 - b_2} + \frac{b_1 \times b_2}{b_1 - b_2} \Delta\mathbf{Q}^* - \frac{b_1 \times b_2}{b_1 - b_2} \times \frac{1}{1 + |\hat{M}|} \mathbf{B}\Delta\mathbf{Q}, \tag{27a}$$

$$\Delta\mathbf{Q}^* = \Delta \begin{pmatrix} \rho \\ \rho u \\ \rho v \\ \rho H \end{pmatrix}, \quad \mathbf{B}\Delta\mathbf{Q} = \left(\Delta\rho - f \frac{\Delta p}{\hat{c}^2} \right) \begin{pmatrix} 1 \\ \hat{u} \\ \hat{v} \\ \hat{H} \end{pmatrix} + \hat{\rho} \begin{pmatrix} 0 \\ \Delta u - n_x \Delta U \\ \Delta v - n_y \Delta U \\ \Delta H \end{pmatrix}, \tag{27b}$$

$$b_1 = \max(0, \hat{U} + \hat{c}, U_{j+1} + c_{j+1}), \quad b_2 = \min(0, \hat{U} - \hat{c}, U_j - c_j). \tag{27c}$$

When compression shock exists, b_1 and b_2 allow Eqs. (27a)–(27c) to capture a shock with no intermediate cell. In case of a non-physical expansion shock, b_1 and b_2 provides enough numerical dissipation to exclude the occurrence of the non-admissible discontinuity. The re-defined signal velocities improve substantially the robustness of the re-formulated scheme, Eqs. (27a)–(27c), in a highly energetic flow, though its positivity cannot be guaranteed.

4.3. Contact discontinuity

In order to resolve boundary layer accurately in viscous flow, it is essential to capture contact discontinuity exactly. The exact solution for a contact discontinuity moving with speed u_c requires that

$$F^{\text{continuity}}_{j+(1/2)} = (1/2)[\rho_j u_j + \rho_{j+1} u_{j+1} - |u_c| \Delta\rho], \text{ i.e., } D^{(\rho)} = |u_c|. \tag{28}$$

After some manipulations, the dissipative coefficient of the modified Roe scheme, Eqs. (27a)–(27c), is obtained as follows.

For $u_j = u_{j+1} = \hat{u}, p_j = p_{j+1} = \hat{p}$, and $\rho_j \neq \rho_{j+1}$

$$D^{(p)} = \left| \frac{u_c}{(\alpha + \beta)(\hat{c} + u_c)} (2\hat{c}u_c + \alpha\hat{c} - \alpha u_c - \beta\hat{c} + \beta u_c + 2\alpha\beta) \right|, \tag{29a}$$

$$b_1 = u_c + \alpha, \quad b_2 = u_2 - \beta (0 \leqslant u_c \leqslant \hat{c}), \tag{29b}$$

$$\alpha = \max(\hat{c}, c_{j+1}), \quad \beta = \max(\hat{c}, c_j). \tag{29c}$$

Three cases of contact discontinuity can be considered.

Case 1: stationary contact discontinuity

$$u_c = 0, D^{(\rho)} = 0. \tag{30}$$

Case 2: moving contact discontinuity with $T_j > T_{j+1}$

$u_c \neq 0, \quad \alpha = \hat{c}, \quad \beta \neq \hat{c},$

$$D^{(p)} = |u_c|. \tag{31}$$

Case 3: moving contact discontinuity with $T_j < T_{j+1}$

$u_c \neq 0, \quad \alpha \neq \hat{c}, \quad \beta = \hat{c},$

$$D^{(p)} = \left| \frac{u_c}{(\alpha + \hat{c})(\hat{c} + u_c)} (3\hat{c}u_c + 3\alpha\hat{c} - \alpha u_c - \hat{c}^2) \right| \neq |u_c|. \tag{32}$$

From the result of case 3, it can be seen that under certain conditions, the re-formulated scheme of Eqs. (27a)–(27c) cannot capture a contact discontinuity exactly. This problem can be readily cured by employing the common speed of sound at a cell interface as follows:

$$b_1 = \max(0, \hat{U} + \hat{c}, U_{j+1} + \hat{c}), \quad b_2 = \min(0, \hat{U} - \hat{c}, U_j - \hat{c}). \tag{33}$$

From the analyses of Section 3.1 to Section 4.3, the newly formulated Roe-based schemes are proposed as follows:

RoeM (Roe scheme with Mach number-based function) 1

$$\mathbf{F}_{j+(1/2)} = \frac{b_1 \times \mathbf{F}_j - b_2 \times \mathbf{F}_{j+1}}{b_1 - b_2} + \frac{b_1 \times b_2}{b_1 - b_2} \Delta\mathbf{Q}^* - \frac{b_1 \times b_2}{b_1 - b_2} \times \frac{1}{1 + |\hat{M}|} \mathbf{B}\Delta\mathbf{Q}, \tag{34a}$$

$$\Delta\mathbf{Q}^* = \Delta \begin{pmatrix} \rho \\ \rho u \\ \rho v \\ \rho H \end{pmatrix}, \quad \mathbf{B}\Delta\mathbf{Q} = \left(\Delta\rho - f \frac{\Delta p}{\hat{c}^2} \right) \begin{pmatrix} 1 \\ \hat{u} \\ \hat{v} \\ \hat{H} \end{pmatrix} + \hat{\rho} \begin{pmatrix} 0 \\ \Delta u - n_x \Delta U \\ \Delta v - n_y \Delta U \\ \Delta H \end{pmatrix}, \tag{34b}$$

$$b_1 = \max(0, \hat{U} + \hat{c}, U_{j+1} + \hat{c}), \quad b_2 = \min(0, \hat{U} - \hat{c}, U_j - \hat{c}). \tag{34c}$$

RoeM 2

$$\mathbf{F}_{j+(1/2)} = \frac{b_1 \times \mathbf{F}_j - b_2 \times \mathbf{F}_{j+1}}{b_1 - b_2} + \frac{b_1 \times b_2}{b_1 - b_2} \Delta\mathbf{Q}^* - g \frac{b_1 \times b_2}{b_1 - b_2} \times \frac{1}{1 + |\hat{M}|} \mathbf{B}\Delta\mathbf{Q}. \tag{34d}$$

Now, the proposed schemes, RoeM 1 and RoeM 2, with the common speed of sound in signal velocities satisfy Eq. (28) for all cases and exclude an expansion shock.

For $u_j = u_{j+1} = \hat{u}, p_j = p_{j+1} = \hat{p}, \rho_j \neq \rho_{j+1}$,

$$D^{(p)}_{RoeM1,2} = |u_c|. \tag{35}$$

4.4. Shock discontinuity

In the situation where a shock discontinuity exists, whether the shock is normal or oblique, $|\hat{U}|$ of Eq. (34c) becomes $\hat{c}$ and $b_1 \times b_2$ is equal to zero due to Roe-averaged values. When a shock discontinuity exists with $U_j > U_{j+1} > 0$,

$$b_1 = \hat{U} + \hat{c}, \quad b_2 = 0, \text{ and } \mathbf{F}_{j+(1/2)} = \mathbf{F}_j.$$

And, for a shock discontinuity with $0 > U_j > U_{j+1}$,

$$b_1 = 0, \quad b_2 = \hat{U} - \hat{c}, \text{ and } \mathbf{F}_{j+(1/2)} = \mathbf{F}_{j+1}.$$

Thus, the RoeM schemes have the capability of capturing a shock discontinuity without intermediate cell, as does Roe's FDS.

5. Numerical results

In this section, we demonstrate the capabilities of the proposed schemes, RoeM 1 and RoeM 2, which are designed according to the criteria mentioned in Section 1, with carefully selected test cases. For higher order extension, the primitive variable interpolation of MUSCL approach is used.

5.1. 1-D test cases

1-D shock tube. This 1-D shock tube test case is similar to the classical Sod test, but with special initial conditions given as $\rho_l = 3,\ u_l = 0.9,\ p_l = 3$ and $\rho_r = 1,\ u_r = 0.9,\ p_r = 1$. Thus, a sonic point exists along rarefaction waves. Roe's FDS yields an entropy violating solution and an expansion shock shown as in Fig. 8. RoeM 1 and RoeM 2 add an optimal amount of dissipation in the expansion region to prevent the formation of an expansion shock.

1-D contact discontinuity. Results of slowly moving contact discontinuity are shown in Fig. 9. The initial conditions are $\rho_l = 10.0,\ u_l = 0.1125,\ p_l = 1$ and $p_r = 0.125,\ u_r = 0.1125,\ p_r = 1$. The iteration count is 500 with the CFL number of 0.85, and the grid points are 100. This condition corresponds to case 3 ($T_l < T_r$) of Eq. (32). As mentioned before, both RoeM 1 and RoeM 2 satisfy Eq. (35) and give accurate results, identical to those from Roe's FDS.

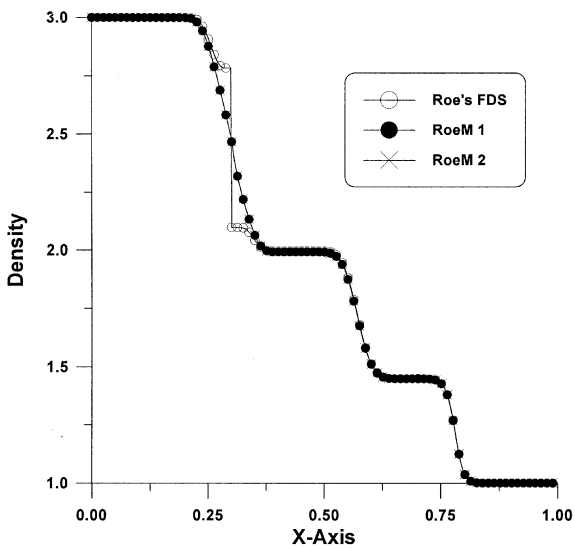

Fig. 8. Sod test case with a sonic point in expansion wave.

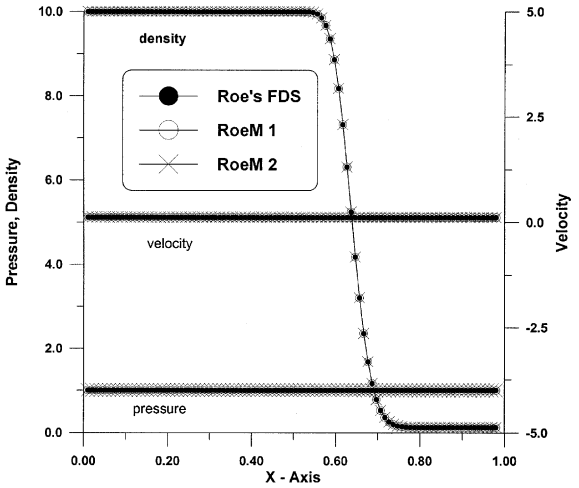

Fig. 9. Slowly moving contact discontinuity with the condition of $T_l < T_r$.

1-D blast wave. This is a highly unsteady problem extensively tested by Woodward and Colella [20]. The initial conditions are $\rho_l = 1.,\ u_l = 0.,\ e_l = 2500.\ (0.0 < x < 0.1),\ \rho_m = 1., u_m = 0.,\ e_m = 0.025\ (0.1 < x < 0.9)$ and $\rho_r = 1.,\ u_r = 0.,\ e_r = 250.\ (0.9 < x < 1.0)$. Two shocks and three contact discontinuities must be resolved with an expansion region in the middle at $t = 0.038$. The results with 1000 cells are shown in Fig. 10. It is evident that noticeable difference is not observed with regard to solution accuracy.

Supersonic expansion test. A supersonic expansion test [3] with the initial conditions of $\rho_l = 1.,\ u_l = -2.,\ e_l = 3.$ and $\rho_r = 1.,\ u_r = 2.,\ e_r = 3.$ is solved to see the behavior of the proposed schemes in highly expansion region. Because Roe's FDS fails in this problem, we compare the results with

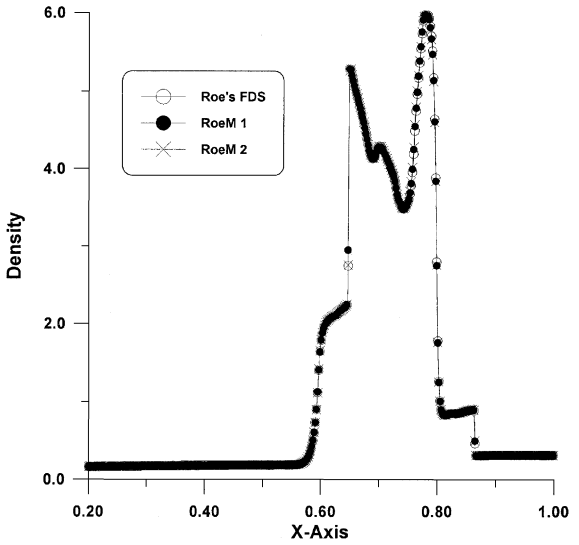

Fig. 10. Woodward–Colella blasting wave test case.

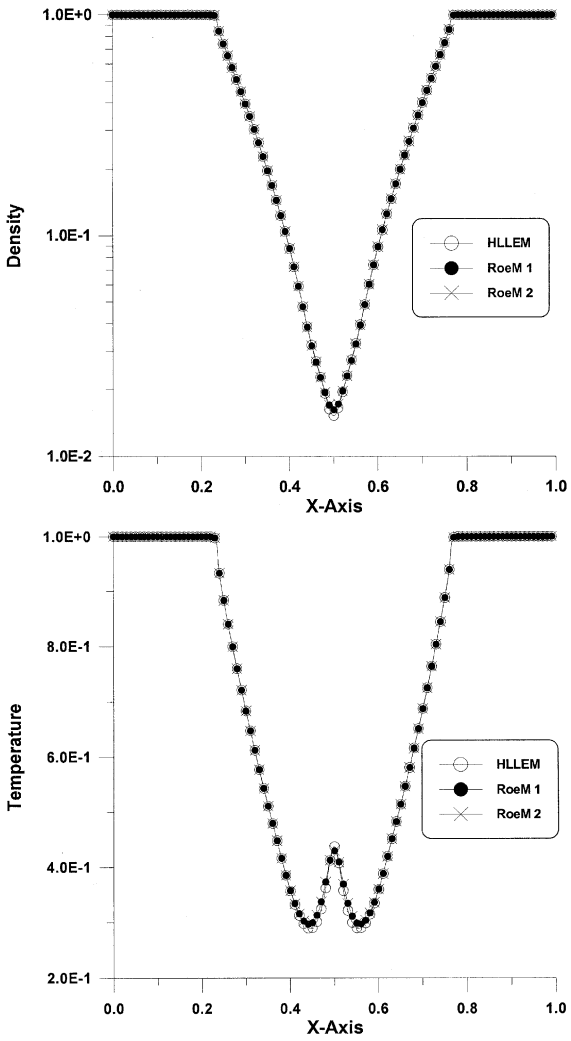

Fig. 11. Supersonic expansion test case.

that of HLLEM. Although the proposed schemes cannot guarantee positively conservativeness, RoeM 1 and RoeM 2 face no difficulty in near vacuum flows as shown Fig. 11.

5.2. Shock instability

5.2.1. Supersonic flow around a half-cylinder

The Carbuncle phenomenon around a blunt body is illustrated in Section 2.3, and it is demonstrated in Section 3.2 that Roe's FDS with the function f does not present a spurious solution. RoeM 1 and RoeM 2 are used to calculate a supersonic inviscid flow around a half-cylinder. The free stream Mach number is 8.0 and the mesh size is 65×113. This problem has the same initial condition and mesh as the test case in Section 2.3. Figure 12 shows pressure contour and shock profiles, which show monotonic behavior. There is

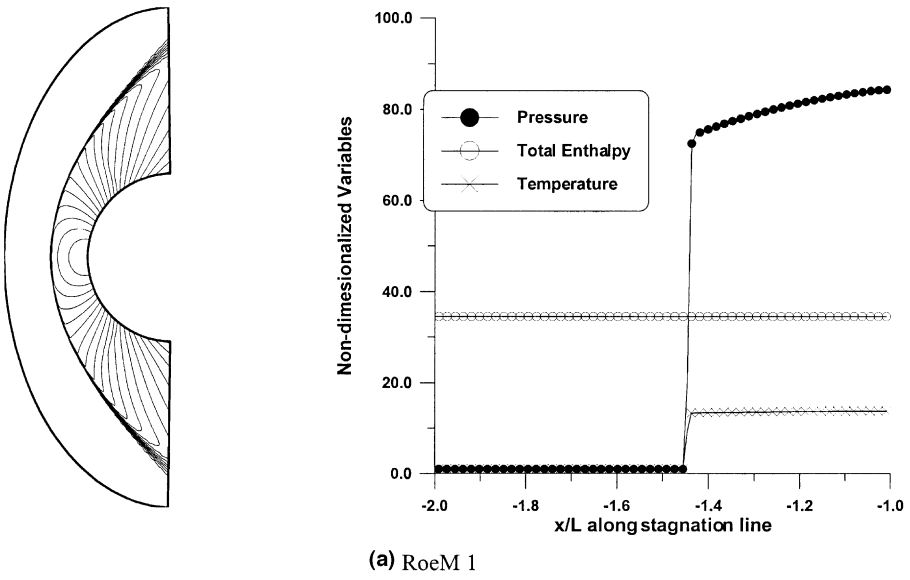

(a) RoeM 1

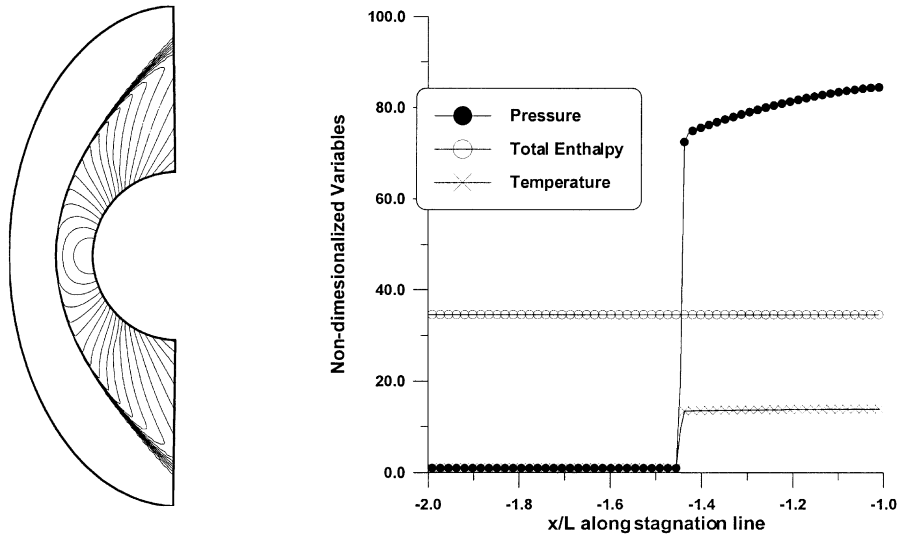

(b) RoeM 2

Fig. 12. Supersonic ($M_\infty = 8.0$) half-cylinder problem: pressure contour and shock profiles along the stagnation streamline.

no symptom of the carbuncle phenomenon. Figure 12 also shows the preservation of total enthalpy, which is important in predicting heat flux accurately at the wall.

5.2.2. Quirk's test-I (odd–even decoupling)

The description of this test case is prescribed in Section 2.1. Roe's FDS amplifies the initial perturbation and completely destroys the normal shock structure as shown in Fig. 1. Figure 13 shows density contour after 3400 iterations. The presented schemes, both RoeM 1 and RoeM 2, clearly capture the shock and initial perturbations do not grow with time.

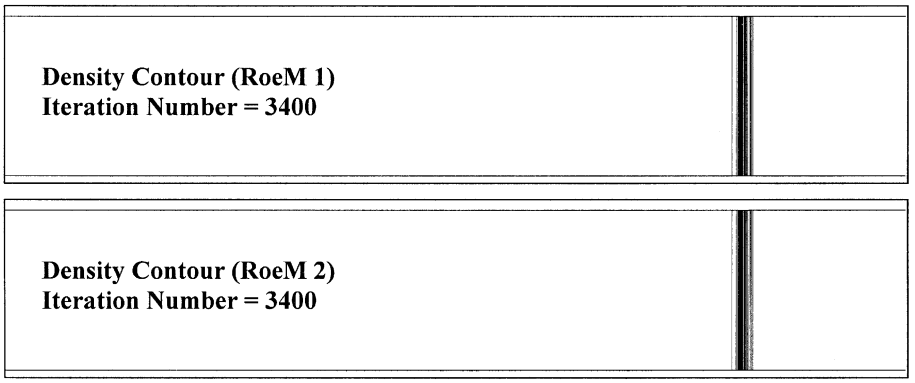

Fig. 13. Quirk's test: odd–even grid decoupling problem with a moving shock of $M_s = 6.0$.

5.2.3. Quirk's test-II (odd–even decoupling)

In this test case, the Quirk's test-I is initially computed using the original Roe's FDS until 550 iterations, and then the solution possessing the shock instability is used as the initial condition for the computation with RoeM 2. Figure 14 shows the evolution of the moving shock at each time. Initial shock profile is being perturbed with Roe's FDS, and it becomes almost impossible to figure out the original shape of the normal shock at 550-iteration step. However, RoeM 2 scheme quickly damps out spurious oscillations and recovers the original shock profile.

5.2.4. The kinked Mach stem

It is well known that Godunov-type schemes show a kinked Mach stem in the double Mach reflection problem. This test is defined by a 30° ramp and a moving shock at $M_s = 5.5$. In Section 2.2, it was examined that Roe's FDS suffers from the kinked Mach stem, and that the instability increases as the mesh is refined. Gressier et al. [13] show that even AUSM+ scheme on a refined mesh can suffer from the kinked Mach stem. Density contours of AUSM+, RoeM 1, and RoeM 2 on a 400×400 mesh are shown in Fig. 15. The results are obtained with first-order spatial accuracy. The kink develops in AUSM+ scheme and RoeM 1 at the principal Mach stem, while RoeM 2 does not show such behavior.

5.2.5. Supersonic corner problem

As a final test case concerning the shock instability, we consider the diffraction of a supersonic moving shock with $M_s = 5.09$, around a 90° corner. Quirk [6] shows the complexity of this flow using grid refinement to resolve the fine details. It is shown that Roe's FDS produces the shock instability along a planar shock wave that is aligned with the grid. Roe's FDS with an entropy fix, HLLE, RoeM 1, and RoeM 2 are applied to calculate this problem. At the 90° corner where the shock is diffracted, Roe's FDS without an entropy fix produces unphysical negative pressure. Many methods are available to cure an expansion shock and instability in the expansion region with an entropy fix. In the present study, the wave speeds of HLLE and HLLEM are used.

$$\lambda_3^* = \max(\lambda_3, U_{j+1} + c_{j+1}), \quad \lambda_4^* = \min(\lambda_4, U_j - c_j), \tag{36a}$$

$$\lambda_3 = \hat{U} + \hat{c}, \quad \lambda_4 = \hat{U} - \hat{c}. \tag{36b}$$

All calculations are made with second-order spatial accuracy using van Albada limiter. The mesh size is 400×400, and the CFL number is 0.4. Figure 16 shows the density contour of each scheme. Roe's FDS

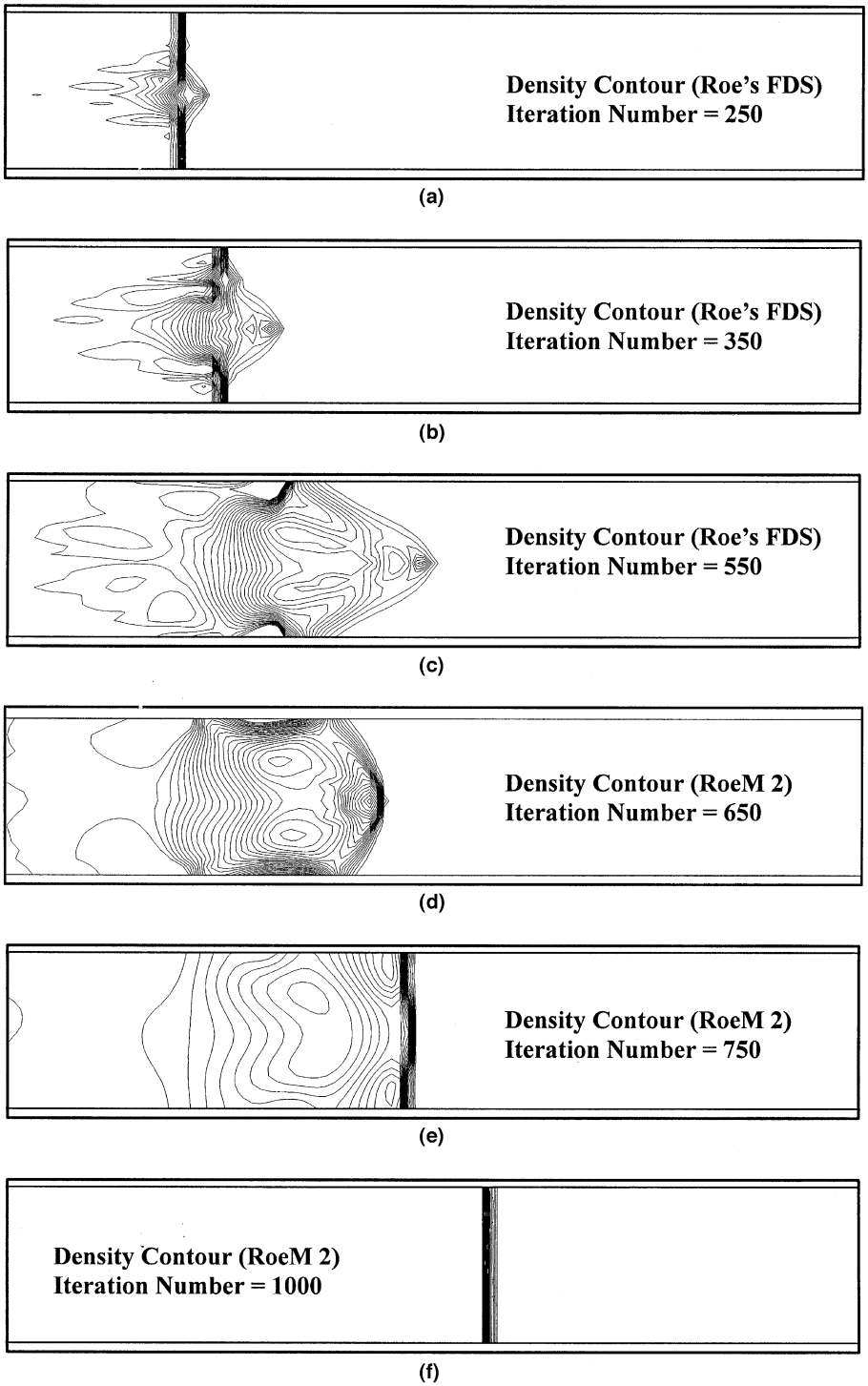

Fig. 14. Quirk's test: computations from the solution of Roe's FDS.

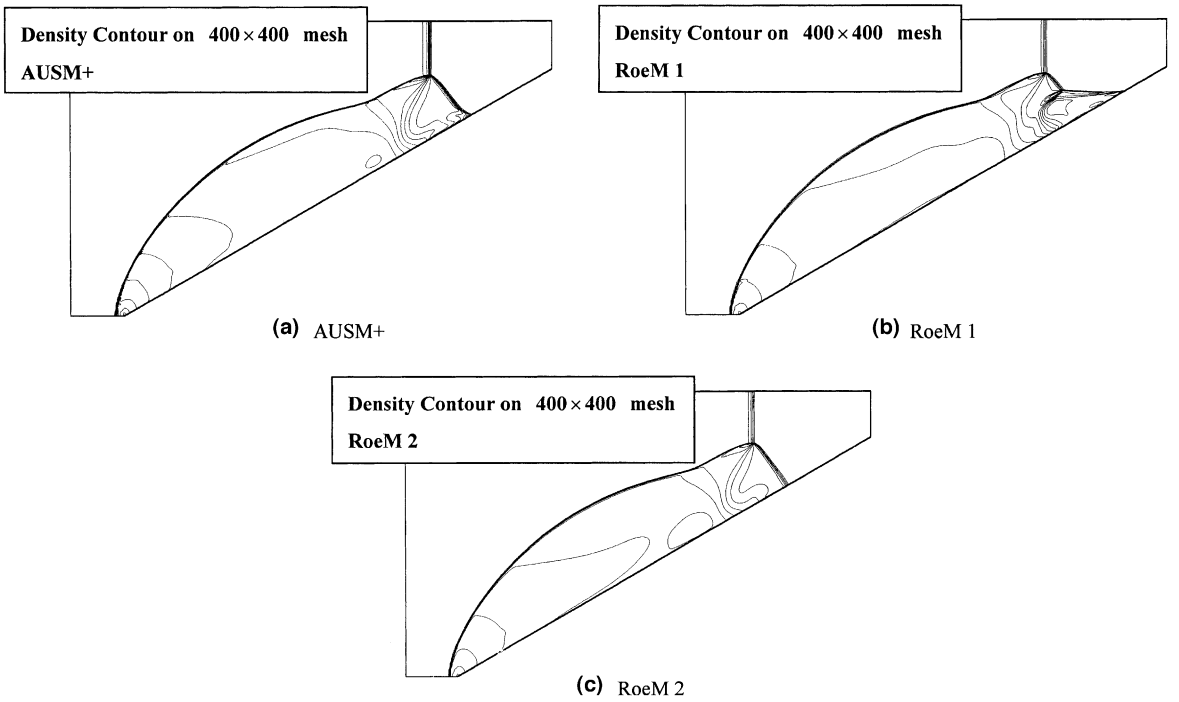

Fig. 15. Density contours of double Mach reflection using AUSM+, RoeM 2 with first-order spatial accuracy.

with the entropy fix to non-linear waves does not experience any particular difficulty in the expansion region, but still shows the shock instability in the primary shock region. HLLE, which considers only non-linear waves, is free from the shock instability and shows good shock-capturing capability as expected, but the flow around the expansion region is somewhat diffused due to numerical dissipation. On the other hand, both RoeM 1 and RoeM 2 show the robustness and accuracy in the expansion region and good shock-capturing ability. There is no symptom of anomaly in the straight stem of the primary shock.

5.3. Viscous flows

5.3.1. Boundary layer over a flat plate

The free stream conditions for laminar boundary layer over a flat plate are as follows:

- Calorically perfect gas.
- $M_\infty = 0.2$.
- $Re = 1.0 \times 10^5$.

The conditions for the computation are as follows:

- Spatial discretization:
  Roe's FDS, RoeM 1, and RoeM 2. Third-order MUSCL without limiter ($\kappa = \frac{1}{3}$).
  The number of grid point $= 81 \times 65$.
- Boundary condition:
  Adiabatic wall condition.

Figure 17 shows the comparison of the velocity profiles of each scheme with the Blasius solution. Like Roe's FDS, RoeM 1, and RoeM 2 produce an excellent agreement with the u and v profiles of the Blasius solution.

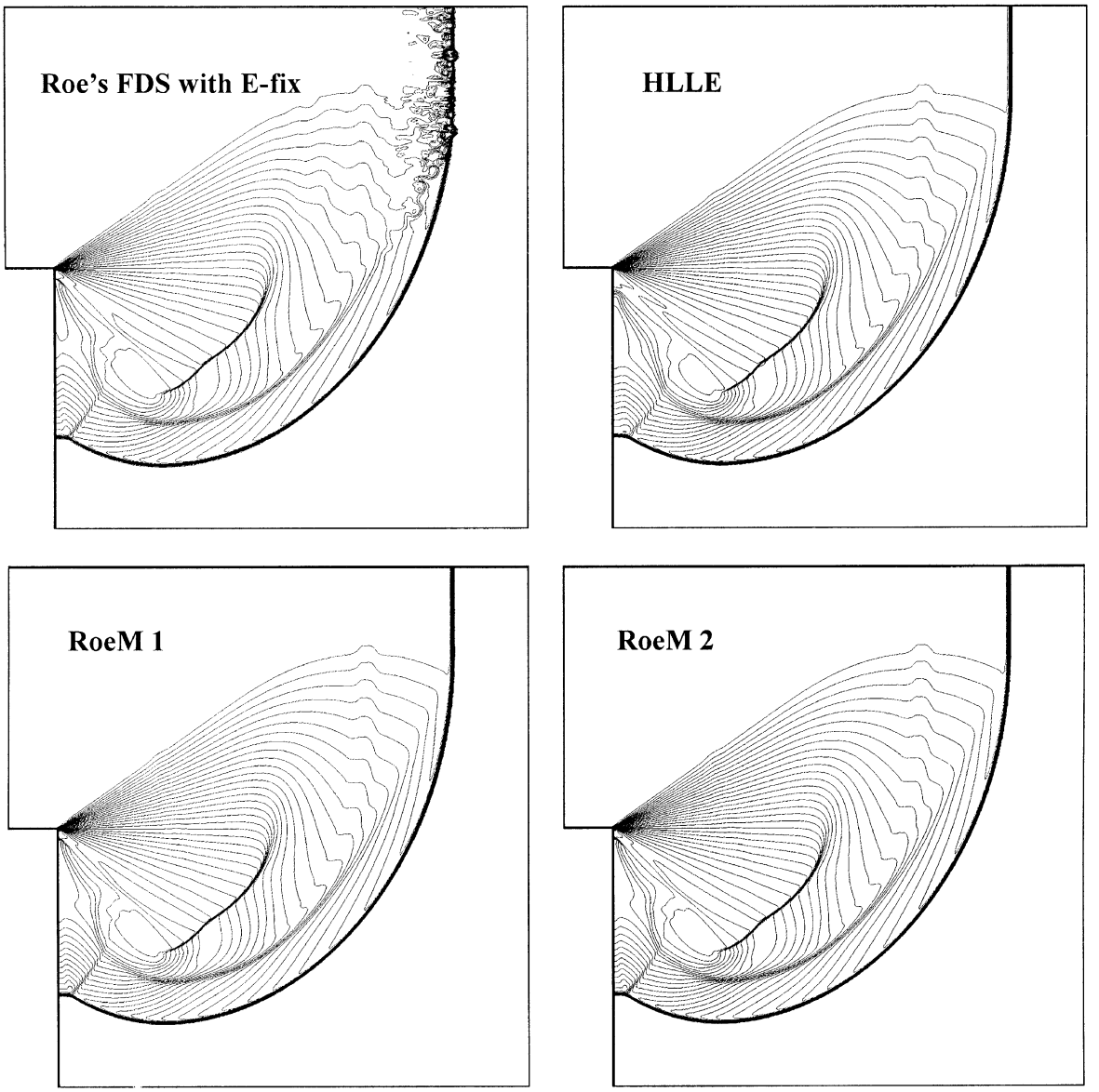

Fig. 16. Density contours of supersonic corner problem on 400×400 mesh using the Roe's FDS with an entropy fix, HLLE, RoeM 1 and RoeM 2.

5.3.2. Shock wave/laminar boundary layer interaction

This test case is a two-dimensional laminar flow, characterized by an oblique shock with an incident angle of 32.585° upon a flat plate causing boundary layer to separate and reattach around the shock-impinging region. The complicated phenomenon provides a good test of validating a scheme before a turbulence model is implemented. The free stream conditions are as follows:

- Calorically perfect gas.
- $M_\infty = 2.0$.

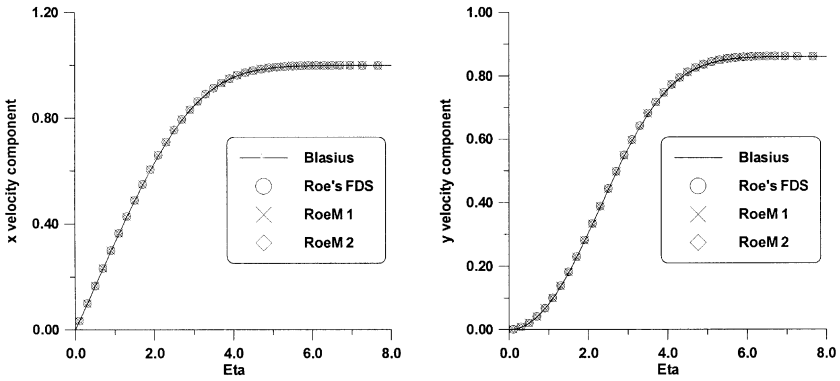

Fig. 17. Boundary layer calculation on a flat plate at $M_\infty = 0.2$ and $Re = 10^4$.

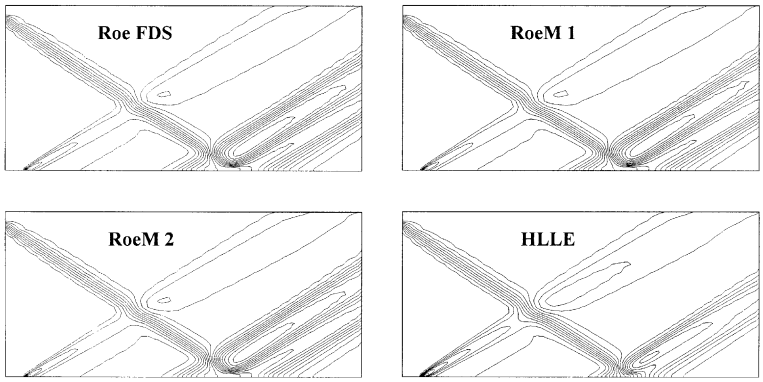

Fig. 18. Pressure contours of shock–boundary interaction problem at $M_\infty = 2.0$ and $Re = 2.96 \times 10^5$.

- $Re = 2.96 \times 10^5$.
- $Pr = 0.72$.
- $\theta_{\text{impinging shock angle}} = 32.585°$.

The conditions for the computation are as follows:

- Spatial discretization:
  Roe's FDS, RoeM 1, RoeM 2 and HLLE. Second-order accuracy with van Leer's limiter.
  The number of grid point $= 105 \times 65$.
- Boundary condition:
  Adiabatic wall condition.

Figure 18 shows the pressure contour of each scheme. Impinging shock and re-circulation region where flow is separated and reattached are well resolved. No spurious oscillation near the oblique shock and wall is observed. In Fig. 19, skin friction coefficients of RoeM 1 and RoeM 2 are compared with the result of Roe's FDS and the experimental data of [21]. It shows that skin friction coefficients of all the proposed schemes are in very good agreement with that of Roe's FDS and experimental data, indicating the capability of the proposed schemes to compute viscous flows involving shock waves and separation. The error histories of the proposed schemes show similar convergent rates to that of Roe's FDS.

5.3.3. Transonic flows around RAE2822 airfoil

This test case is concerned with viscous turbulent flows around the RAE2822 airfoil at the transonic regime. The free stream conditions of the first case are as follows:

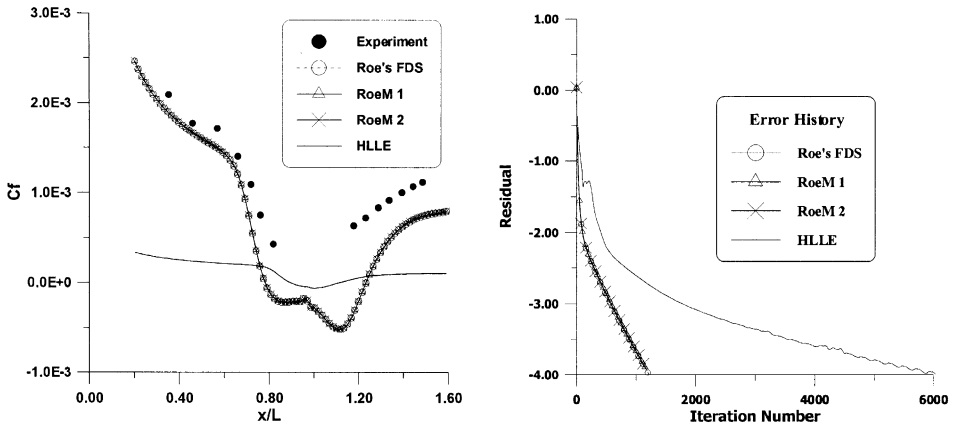

Fig. 19. Skin friction coefficients and error histories of shock–boundary interaction problem at $M_\infty = 2.0$ and $Re = 2.96 \times 10^5$.

- Calorically perfect gas.
- $M_\infty = 0.73$.
- $Re = 6.5 \times 10^6$.
- $Pr = 0.72$.
- $\alpha = 2.19°$.

  The conditions for the computation are as follows:
- Spatial discretization:

  Roe FDS, RoeM 1, and RoeM 2. Second-order accuracy with van Leer's limiter.

  The number of grid point $= 241 \times 48$, C-type mesh.
- Boundary condition:

  Non-slip adiabatic wall condition.

The condition corresponds to the experimental Case 9 in [22]. The Baldwin–Lomax turbulence model is used. The flow is assumed to be fully turbulent without transition near the leading edge. Figure 20 shows Cp distribution and error history. Differences between the proposed schemes and Roe's FDS are hardly noticeable, and the result shows a fairly accurate Cp distribution compared with experimental data.

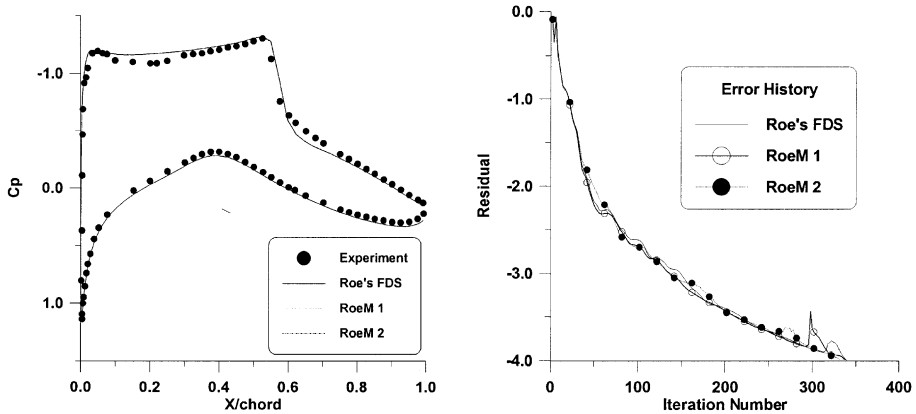

Fig. 20. Cp distribution and error history around RAE2822 airfoil at $M_\infty = 0.73$, $\alpha = 2.79°$ and $Re = 6.5 \times 10^6$ with the Baldwin–Lomax turbulence model.

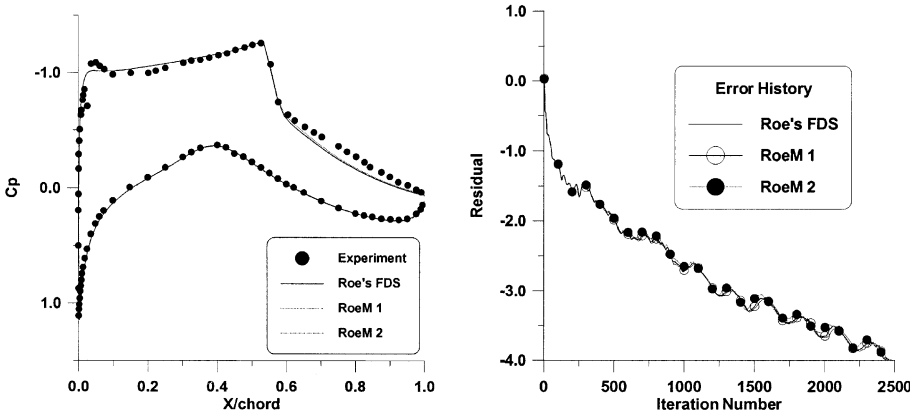

Fig. 21. Cp distribution and error history around RAE2822 airfoil at $M_\infty = 0.75$, $\alpha = 2.81°$ and $Re = 6.2 \times 10^6$ with the $k\omega$-SST turbulence model.

The second case has the free stream conditions as follows:

- Calorically perfect gas.
- $M_\infty = 0.75$.
- $Re = 6.2 \times 10^6$.
- $Pr = 0.72$.
- $\alpha = 2.81°$.

The conditions for the computation are as follows:

- Spatial discretization:
  Roe FDS, RoeM 1, and RoeM 2. Second-order accuracy with van Leer's limiter.
  The number of grid point $= 241 \times 65$, O-type mesh.
- Boundary condition:
  Non-slip adiabatic wall condition.

This condition corresponds to the experimental Case 10 in [22]. The two-equation $k\omega$-SST turbulence model by Menter [23] is adopted. Figure 21 shows the comparison of Cp distribution and error history with Roe's FDS and experimental data, which validates again the performance of RoeM 1 and RoeM 2. As can be seen from the computed results, the present schemes work well with popular turbulence models.

5.3.4. Hypersonic flow around a blunt body

A hypersonic blunt body problem is chosen in order to examine the effects of a strong shock discontinuity and large gradients in boundary layer. In computing this problem, the primary concern is the accurate prediction of surface heating rate at the wall. The free stream conditions are as follows:

- Calorically perfect gas.
- $M_\infty = 16.34$.
- $p_\infty = 82.95\ (\mathrm{N/m^2})$.
- $\rho_\infty = 5.557 \times 10^{-3}\ (\mathrm{kg/m^3})$.
- $\mu_\infty = 3.369 \times 10^{-6}\ (\mathrm{kg/m\,s^2})$.
- $T_\infty = 52\,\mathrm{K}$.
- $T_{\mathrm{wall}} = 294.4\,\mathrm{K}$.
- $Re = 1.4972 \times 10^5$.
- $Pr = 0.72$.

The conditions for the computation are as follows:

- Spatial discretization:
  RoeM 1 and RoeM 2. Third-order MUSCL with minmod limiter ($\beta = 1,\ \kappa = \frac{1}{3}$).
  The number of grid point $= 65 \times 113$.
- Boundary condition:
  Constant temperature wall.

Roe's FDS is not used for this test case due to the carbuncle phenomenon, and the computed results of RoeM 1 an RoeM 2 are compared with the experimental data [24]. Figure 22 shows shock profiles of each scheme along the stagnation line. The left figures are the results along the stagnation line and the right shows the results inside boundary layer. Pressure and temperature profiles maintain monotonicity across the shock. In boundary layer, no spurious oscillation of flow properties is observed. The number of grid point in boundary layer is sufficient to resolve temperature change accurately, i.e., heat flux. Figure 23 shows surface heating rates and skin friction coefficients of the proposed schemes, indicating a very good agreement with experimental data.

5.3.5. 3-D viscous calculation around ONERA M6 wing

As a final test case, the flow over the ONERA M6 wing with a sweepback angle of 30° and aspect ratio of 3.18 is computed. RoeM 1 and RoeM 2 schemes are easily extended to 3-dimensional flows. Convection terms in the z-direction are included as follows:

RoeM 1

$$\mathbf{F}_{j+(1/2)} = \frac{b_1 \times \mathbf{F}_j - b_2 \times \mathbf{F}_{j+1}}{b_1 - b_2} + \frac{b_1 \times b_2}{b_1 - b_2}\Delta\mathbf{Q}^* - \frac{b_1 \times b_2}{b_1 - b_2} \times \frac{1}{1 + |\hat{M}|}\mathbf{B}\Delta\mathbf{Q}, \tag{37a}$$

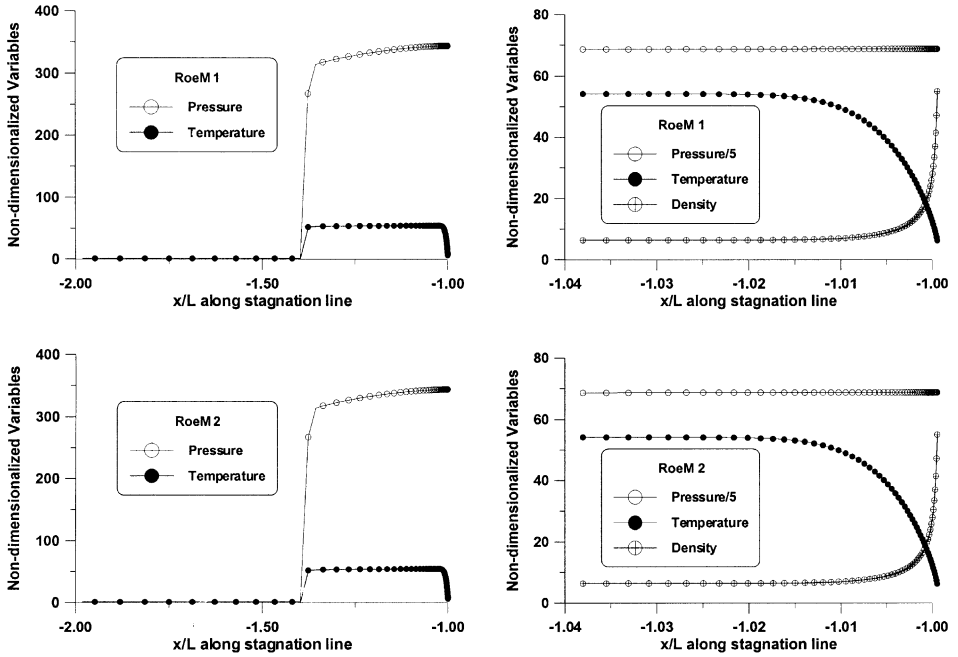

Fig. 22. Shock profiles along the stagnation line.

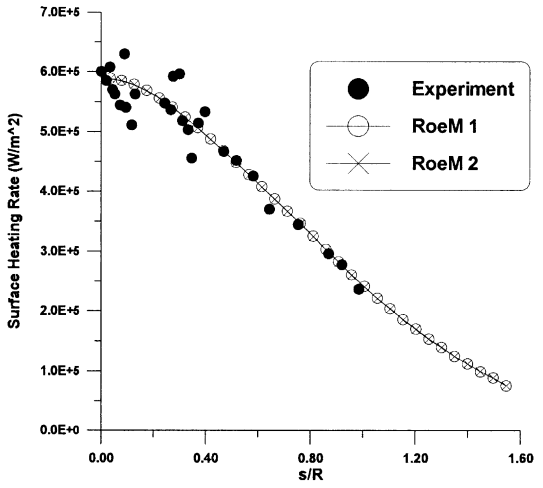

Fig. 23. Surface heating rates over a half-cylinder at $M_\infty = 16.32$ and $Re = 1.4972 \times 10^5$ with constant wall temperature $T_{\text{wall}} = 294.4\,\text{K}$.

$$\Delta\mathbf{Q}^* = \Delta\begin{pmatrix}1\\ \rho u\\ \rho v\\ \rho w\\ \rho H\end{pmatrix},\quad \mathbf{B}\Delta\mathbf{Q} = \left(\Delta\rho - f\frac{\Delta p}{\hat{c}^2}\right)\begin{pmatrix}1\\ \hat{u}\\ \hat{v}\\ \hat{w}\\ \hat{H}\end{pmatrix} + \hat{\rho}\begin{pmatrix}0\\ \Delta u - n_x\Delta U\\ \Delta v - n_y\Delta U\\ \Delta w - n_z\Delta U\\ \Delta H\end{pmatrix}, \tag{37b}$$

$$b_1 = \max(0, \hat{U} + \hat{c}, U_{j+1} + \hat{c}),\quad b_2 = \min(0, \hat{U} - \hat{c}, U_j - \hat{c}). \tag{37c}$$

RoeM 2

$$\mathbf{F}_{j+(1/2)} = \frac{b_1 \times \mathbf{F}_j - b_2 \times \mathbf{F}_{j+1}}{b_1 - b_2} + \frac{b_1 \times b_2}{b_1 - b_2}\Delta\mathbf{Q}^* - g\frac{b_1 \times b_2}{b_1 - b_2} \times \frac{1}{1 + |\hat{M}|}\mathbf{B}\Delta\mathbf{Q}. \tag{37d}$$

$$f = \begin{cases} 1 & \hat{u}^2 + \hat{v}^2 = 0,\\ |\hat{M}|^h & \text{elsewhere.}\end{cases} \tag{37e}$$

$$\begin{aligned} h = 1 - \min\big(&P_{i,j+(1/2),k}, P_{i-(1/2),j,k}, P_{i+(1/2),j,k}, P_{i-(1/2),j+1,k}, P_{i+(1/2),j+1,k}, P_{i,j,k-(1/2)},\\ &P_{i,j,k+(1/2)}, P_{i,j+1,k-(1/2)}, P_{i,j+1,k+(1/2)}\big), \end{aligned} \tag{37f}$$

$$P_{i,j+(1/2),k} = \min\left(\frac{p_{i,j,k}}{p_{i,j+1,k}}, \frac{p_{i,j+1,k}}{p_{i,j,k}}\right). \tag{37g}$$

$$g = \begin{cases} |M|^{1-\min\left(\frac{P_j}{P_{j+1}}, \frac{P_{j+1}}{P_j}\right)}, & M \neq 0,\\ 1, & M = 0.\end{cases} \tag{37h}$$

The free stream conditions are as follows:

- Calorically perfect gas.
- $M_\infty = 0.84$.
- $Re = 1.46 \times 10^7$.
- $Pr = 0.72$.
- $\alpha = 3.06°$.

The conditions for the computation are as follows:

- Spatial discretization:

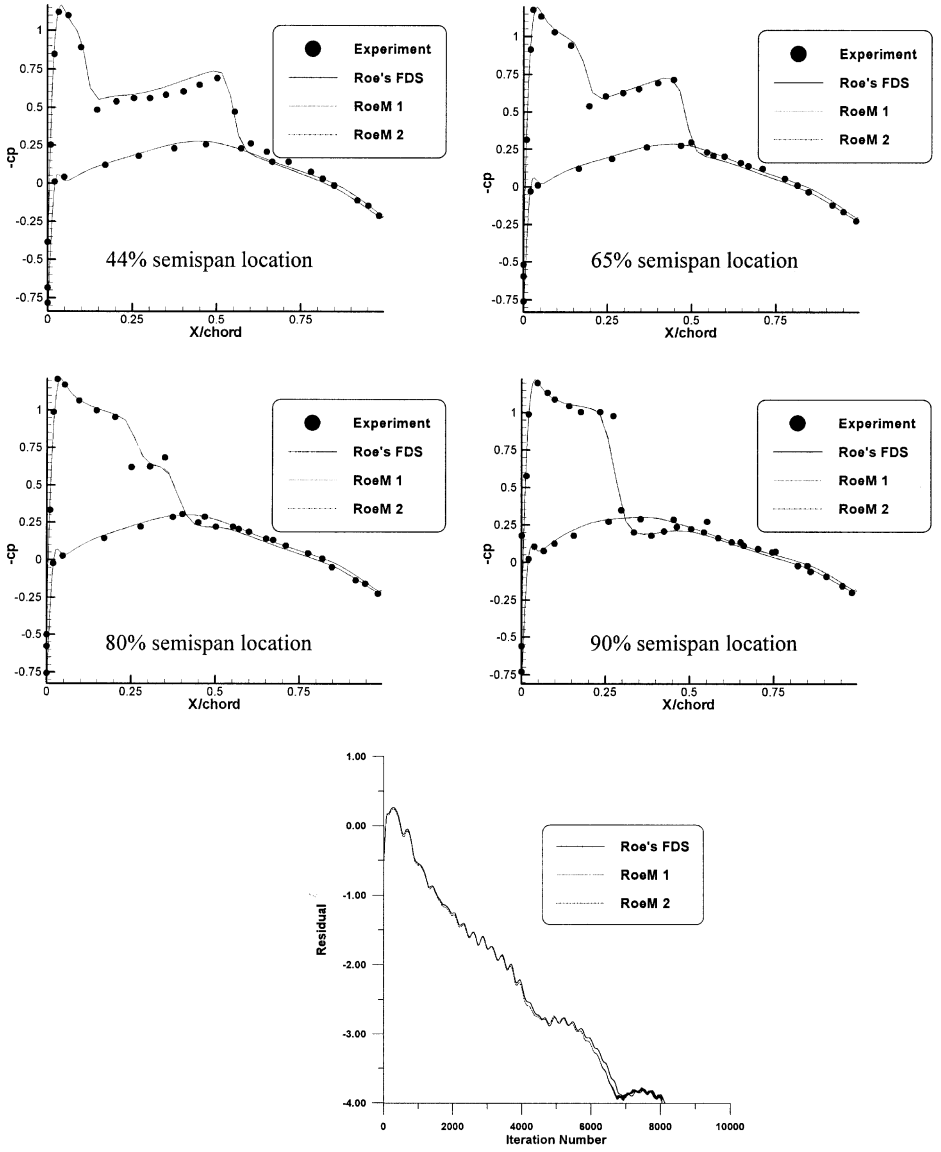

Fig. 24. Cp distribution and error history over ONERA M6 wing at $M_\infty = 0.84$, $\alpha = 3.06°$ and $Re = 1.46 \times 10^7$ with the $k\omega$-SST turbulence model.

Table 1
Computational cost of proposed schemes

Roe's FDS	RoeM 1	RoeM 2
1	1.2	1.2

Roe FDS, RoeM 1, and RoeM 2. Third-order accuracy with Koren limiter. $k\omega$-SST turbulence model. The number of grid point $= 143 \times 33 \times 65$ O–O type.

- Boundary condition:
  Non-slip adiabatic wall condition.

Computed results by RoeM 1 and RoeM 2 are compared with that by Roe's FDS and the experiment [25]. In Fig. 24, error history and surface Cp distributions at four spanwise positions of 44%s, 65%s, 80%s, and 90%s are compared with each other. The computed results show a good agreement with Roe's FDS and experimental one.

Finally, the computational efficiency of the proposed schemes is presented. Due to the calculations of control functions f and g, the proposed schemes take a relatively more computing time than Roe's FDS. Table 1 shows the relative computational cost. Considering the various desirable properties and robustness, however, the computational burden is clearly compensated.

6. Concluding remarks

Starting from the original Roe's FDS scheme, newly formulated shock-stable Roe-based schemes, Roe with Mach number-based function schemes (RoeM 1 and RoeM 2), are developed. In order to control the feeding rate of pressure fluctuation in the numerical mass flux, which is considered to be the source of the shock instability, a control function f is introduced. The function f has the role of reducing the rate at which pressure perturbation feeds density field. Another function g in RoeM 2 has the role of increasing the damping rate of density perturbation and controlling the pressure perturbation simultaneously. Improved wave speed is introduced to remedy expansion shock and numerical instability in the expansion region, while the capability to capture contact discontinuity exactly is still retained. For the accurate prediction of surface heat transfer rate, RoeM schemes are also designed to preserve total enthalpy. Although control functions f and g are very simple, extensive computational tests performed in the present paper confirm that the proposed schemes are able to solve a wide range of aerodynamic problems, accurately and without the shock instability, especially where strong physical discontinuities or gradients of flow properties exist. The numerical results with RoeM 1 and RoeM 2 shows that the shock instability is strongly dependent on pressure contribution to the numerical mass flux, and the shock stability can be compatible with the exact capture of the contact discontinuity.

Acknowledgements

The authors appreciate the financial support by Agency for Defense Development (ADD) and by the Brain Korea-21 Program for the Mechanical and Aerospace Engineering Research at Seoul National University.

References

[1] S.K. Godunov, A difference scheme for the numerical computation of discontinuous solutions of hydrodynamic equations, Math. Sbornik 47 (1959) 271.

[2] P.L. Roe, Approximate Riemann solvers, parameter vectors, and difference schemes, J. Comput. Phys. 43 (1981) 357.
[3] B. Einfeldt, C.D. Munz, P.L. Roe, B. Sjögreen, On Godunov-Type methods near low densities, J. Comput. Phys. 92 (1991) 273.
[4] S. Osher, S. Chakravarthy, Upwind scheme and boundary conditions with applications to Euler equations in generalized geometries, J. Comput. Phys. 50 (1983) 447.
[5] K.M. Peery, S.T. Imlay, Blunt-body flow simulations, AIAA Paper 88-2904, 1988.
[6] J.J. Quirk, A contribution to the great Riemann solver debate, Int. J. Numer. Meth. Fluids 18 (1994) 555.
[7] Y. Wada, M.S. Liou, An accurate and robust flux splitting scheme for shock and contact discontinuities, SIAM J. Sci. Comput. 18 (3) (1997) 633.
[8] H.C. Lin, Dissipation addition to flux-difference splitting, J. Comput. Phys. 117 (1995) 20.
[9] M.S. Liou, Mass flux schemes and connection to shock instability, J. Comput. Phys. 160 (2000) 623.
[10] K. Xu, Gas-kinetic schemes for unsteady compressible flow simulations, VKI LS 1998-03 (1998) 1.
[11] R. Sanders, E. Morano, M.C. Druguet, Multidimensional dissipation for upwind schemes: stability and applications to gas dynamics, J. Comput. Phys. 145 (1998) 511.
[12] J. Gressier, J.M. Moschetta, Robustness versus accuracy in shock-wave computations, Int. J. Numer. Meth. Fluids. 33 (2000) 313.
[13] J.C. Robinet, J. Gressier, G. Casalis, J.M. Moschetta, Shock wave instability and the carbuncle phenomenon: same intrinsic origin?, J. Fluid Mech. 417 (2000) 237.
[14] M. Pandolfi, D. D'Ambrosio, Numerical instabilities in upwind methods: analysis and cures for the "Carbuncle" phenomenon, J. Comput. Phys. 166 (2001) 271.
[15] K.H. Kim, O.H. Rho, An improvement of AUSM schemes by introducing the pressure-based weight functions, Computers & Fluids 27 (3) (1998) 311.
[16] K.H. Kim, C. Kim, O.H. Rho, Methods for the accurate computations f hypersonic flows I. AUSMPW + Scheme, J. Comput. Phys. 174 (2001) 38.
[17] K.H. Kim, C. Kim, Uncertainty in the Euler equations and numerical instability, prepared for publication 2002.
[18] A. Jameson, Analysis and design of numerical schemes for gas dynamics 2. Artificial diffusion and discrete shock structure, Int. J. Comput. Fluid Dynamics 5 (1995) 1.
[19] D. Hänel, On the accuracy of upwind schemes in the solutions of the Navier–Stokes equations, AIAA Paper 87-1105-CP, 1987.
[20] P. Woodward, P. Collela, The numerical simulation of two-dimensional fluid flow with strong shocks, J. Comput. Phys. 54 (1984) 115.
[21] R.J. Hakkinen, I. Greber, L. Trilling, S.S. Abarnel, The interaction of an oblique shock wave with a laminar boundary layer, Tr 57-1, Fluid Dynamics Research Group, MIT, May 1957.
[22] P.H. Cook, M.A. McDonald, M.C.P. Firmin, AIRFOIL RAE 2822 pressure distributions, boundary layer and wake measurements, AGARD Advisory Report 138, 1979.
[23] F.R. Menter, Two-equation Eddy-viscosity turbulence models for engineering applications, AIAA J. 32 (1994) 1598.
[24] M.S. Holden, A.R. Weiting, J.R. Moselle, C. Glass, Studies of aerothermal loads generated in regions of shock/shock interaction in hypersonic flow, AIAA Paper 88-0047, Jan 1988.
[25] V. Schmitt, F. Charpin, Pressure distribution on the ONERA M6 Wing at Transonic Mach Numbers, AGARD-AR-138, 1979.